

Neuron

The Dynamic Localization of Cytoplasmic Dynein in Neurons Is Driven by Kinesin-1

Highlights

- Dynein localization is dynamic prior to axon specification
- Dynein is enriched distally in axons via slow axonal transport
- Anterograde trafficking of dynein is driven by a direct interaction with kinesin-1
- Slow transport of cytosolic cargos involves transient links to processive motors

Authors

Alison E. Twelvetrees, Stefano Pernigo, Anneri Sanger, ..., Roberto A. Steiner, Mark P. Dodding, Erika L.F. Holzbaur

Correspondence

holzbaur@mail.med.upenn.edu

In Brief

Twelvetrees et al. examine dynein localization in neurons and find that dynein dynamically relocates among neurites prior to axon specification. Following specification, dynein is constitutively trafficked down the axon via transient, but direct, interactions with the processive motor kinesin-1.



The Dynamic Localization of Cytoplasmic Dynein in Neurons Is Driven by Kinesin-1

Alison E. Twelvetrees,^{1,2} Stefano Pernigo,³ Anneri Sanger,³ Pedro Guedes-Dias,¹ Giampietro Schiavo,² Roberto A. Steiner,³ Mark P. Dodding,³ and Erika L.F. Holzbaur^{1,*}

¹Department of Physiology, Perelman School of Medicine, University of Pennsylvania, Philadelphia, PA 19104-6085, USA

²Molecular NeuroPathobiology Laboratory, Sobell Department of Motor Neuroscience & Movement Disorders, UCL Institute of Neurology, University College London, London, WC1N 3BG, UK

³Randall Division of Cell and Molecular Biophysics, King's College London, London, SE1 1UL, UK

*Correspondence: holzbaur@mail.med.upenn.edu

<http://dx.doi.org/10.1016/j.neuron.2016.04.046>

SUMMARY

Cytoplasmic dynein, the major motor driving retrograde axonal transport, must be actively localized to axon terminals. This localization is critical as dynein powers essential retrograde trafficking events required for neuronal survival, such as neurotrophic signaling. Here, we demonstrate that the outward transport of dynein from soma to axon terminal is driven by direct interactions with the anterograde motor kinesin-1. In developing neurons, we find that dynein dynamically cycles between neurites, following kinesin-1 and accumulating in the nascent axon coincident with axon specification. In established axons, dynein is constantly transported down the axon at slow axonal transport speeds; inhibition of the kinesin-1-dynein interaction effectively blocks this process. In vitro and live-imaging assays to investigate the underlying mechanism lead us to propose a new model for the slow axonal transport of cytosolic cargos, based on short-lived direct interactions of cargo with a highly processive anterograde motor.

INTRODUCTION

In neurons most pre-synaptic proteins are synthesized in the soma and are then transported long distances to reach their site of action. The continuous synthesis and delivery of new axonal proteins is essential to neuronal function (Kleim et al., 2003). In vivo pulse chase labeling experiments identified two major forms of anterograde axonal transport (see Roy, 2014 for recent review): a fast component (FC) associated with vesicular organelles moving between 50–200 mm/day and a slow component of cytoskeletal and cytoplasmic proteins moving 0.2–10 mm/day, which can be further subdivided into slow component a (SCa) and slow component b (SCb). The transit of new axonal and synaptic constituents via slow transport can take up to a year for cells with extended axons such as human motor neurons. However, at least three times the amount of protein is delivered to pre-synapses by slow compared to fast transport

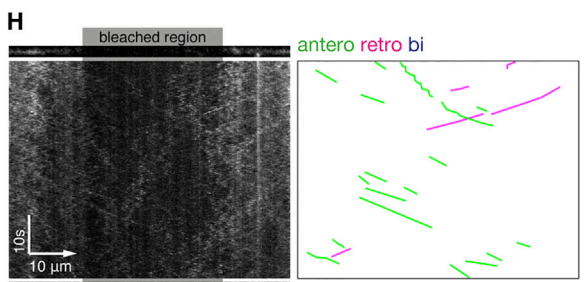
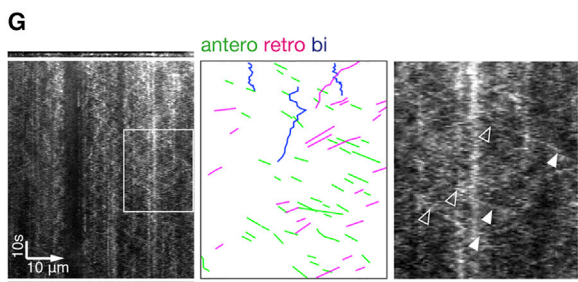
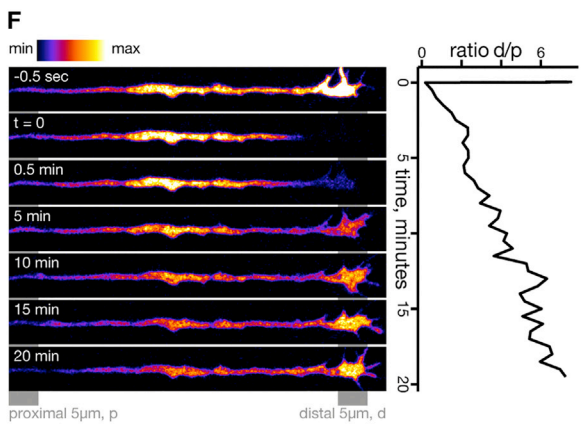
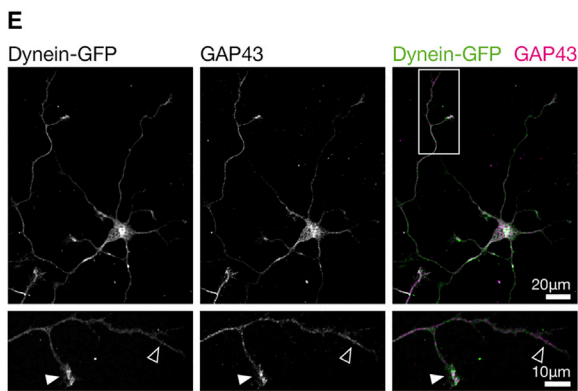
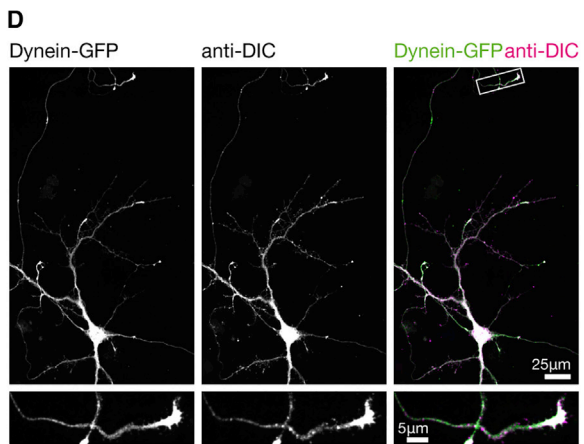
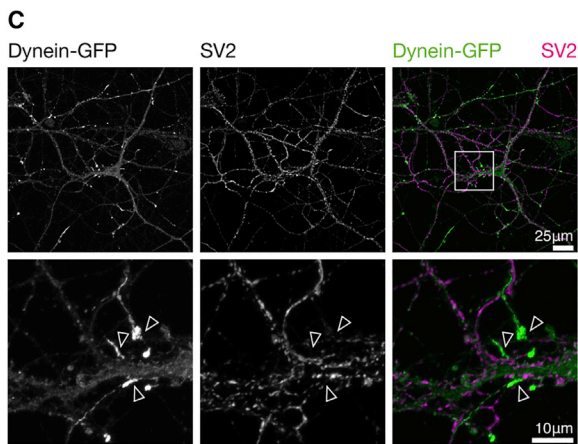
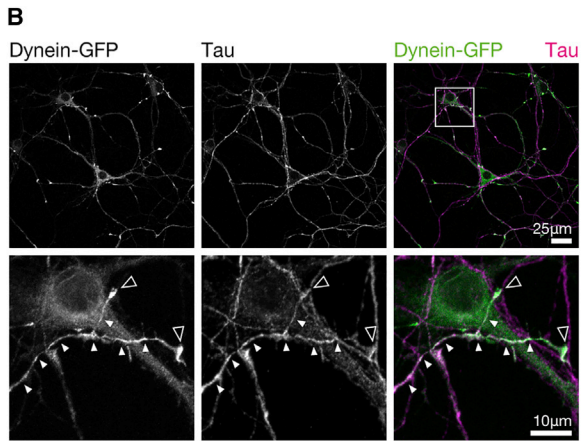
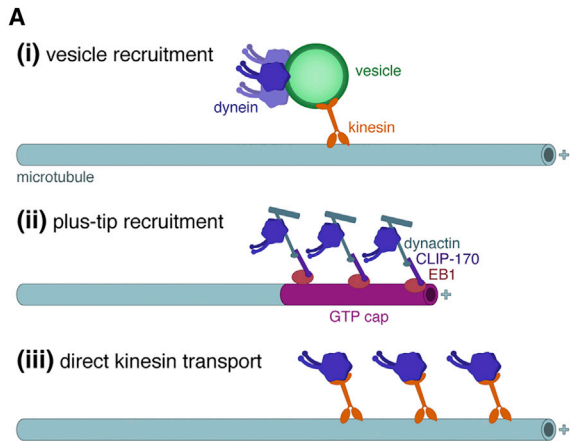
(Garner and Mahler, 1987), making this the major protein delivery system.

There has been significant progress in our understanding of fast axonal transport (Maday et al., 2014), but slow axonal transport has been more difficult to study. Groundbreaking work on neurofilament transport demonstrated that while overall rates of slow transport are orders of magnitude less than fast transport, there are no slow transport-specific motor proteins (Brown et al., 2005; Roy et al., 2000; Wang et al., 2000); instead, slow transport relies on the same microtubule motors that mediate fast vesicular transport (He et al., 2005; Wagner et al., 2004). Consequently, instantaneous velocities for neurofilaments are similar to those measured for vesicular cargos, but overall transport rates are dominated by long off-track times in a “stop and go” model for transport (Brown et al., 2005).

The slow transport of diffuse cytosolic proteins of SCb has been even more difficult to study, as there is no discrete unit to track through time. Recent success has been achieved using photoactivation to monitor SCb proteins synapsin and CaMKII (Scott et al., 2011). This work led to the proposal that presynaptic proteins transiently aggregate and associate with passing vesicles in a “dynamic-recruitment” model (Scott et al., 2011; Tang et al., 2013). However, the molecular mechanisms driving these dynamics remain undefined.

Here, we focus on the anterograde axonal transport of cytoplasmic dynein. Metabolic labeling studies indicate that ~80% of newly synthesized dynein moves outward as a component of slow axonal transport at SCb velocities (1–10 mm/day) (Dillman et al., 1996a, 1996b). Cytoplasmic dynein is the major retrograde motor in axons, yet it cannot drive its own localization to the axon terminal because the uniform microtubule polarity in axons directs active dynein back to the soma. Dynein is essential for many axonal functions including: growth cone extension (Grabham et al., 2007; Myers et al., 2006); axon elongation (Roossien et al., 2014); retrograde neurotrophic signaling (Heerssen et al., 2004; Yano et al., 2001); and autophagy (Maday et al., 2012). Consequently, mutations in dynein lead to neurodevelopmental and neurodegenerative phenotypes in both humans and mice (Schiavo et al., 2013). Although the distal localization of dynein in the axon is essential to normal neuronal function, how this is achieved is unknown.

There are three mechanisms that could describe the anterograde transport of dynein on microtubules (Figure 1A): (1) transport of dynein on vesicles, (2) “surfing” of dynein on polymerizing



(legend on next page)

microtubule plus ends, and (3) direct transport by kinesin. While a small fraction of dynein motors are trafficked down the axon on fast-moving vesicles (Dillman et al., 1996a, 1996b), this population of motors is stably attached to organelles (Encalada et al., 2011; Hendricks et al., 2010) and unavailable for other essential dynein-driven functions. Alternatively, anterograde transport of dynein could result from dynein recruitment to growing microtubule plus ends via binding to the plus-end-tracking proteins (+TIPs) EB1 and CLIP-170 through dynactin (Moughamian et al., 2013; Nirschl et al., 2016). Due to their uniform polarity, polymerizing microtubules within the axon produce +TIP comets that move away from the soma; dynein could potentially “surf” the +TIP wave toward the axon tip. Finally, in support of the direct recruitment model, a minimal complex for dynein transport by kinesin was recently reconstituted from yeast proteins (Roberts et al., 2014), indicating that this scenario is also possible.

To test these possibilities, we used a dynein-GFP mouse: a knockin model with tandem GFP and FLAG tags fused in frame to the C terminus of the neuron-specific isoform of the dynein intermediate chain (DIC1) (Zhang et al., 2013). Thus, tagged DIC1 is expressed at endogenous levels and incorporates into the multi-subunit dynein complex to produce functional motors (Ayloo et al., 2014; Zhang et al., 2013). We used live cell imaging at different spatiotemporal scales to define the anterograde movement of the dynein-GFP population, in combination with *in vitro* biochemistry and single molecule assays to identify a motile dynein:kinesin complex. These studies provide new mechanistic insight into the active transport and localization of an essential neuronal motor by demonstrating a robust kinesin-dependent, but non-vesicular, translocation of dynein along the axon of primary hippocampal neurons.

RESULTS

Dynein Preferentially Accumulates in Distal Axons throughout Development

As an important first step, we wanted to characterize the distribution of cytoplasmic dynein in our model system of primary hippocampal neurons isolated from the dynein-GFP knockin mouse. In hippocampal neurons at 8 days *in vitro* (DIV), dynein-GFP was present throughout the somatodendritic and axonal compartments. However, the distribution was not homogeneous as there was a striking accumulation of dynein-GFP in

the distal ends of axons, appearing as many bright puncta in larger fields of view (Figures 1B–1D, top panels). Axonal accumulation of dynein-GFP was confirmed by co-staining neurons with antibodies to GFP and the axonal marker tau. While not co-localized, both proteins were consistently enriched within the same cellular compartment (Figure 1B, empty arrowheads indicate dynein in axon terminals). We did not observe co-localization of dynein-GFP puncta with the pre-synaptic marker SV2 either at 8 DIV (Figure S1A) or in established cultures at 21 DIV (Figure 1C). These observations suggest that dynein-GFP is preferentially localized to growth cones and the distal axon, which we confirmed by co-staining stage 3 (DIV3) dynein-GFP hippocampal neurons with anti-GFP and the early growth cone marker GAP43 (Figure 1E, filled arrowhead). Thus, dynein accumulates in the distal axon, far from its site of synthesis. This distal localization was not limited to the GFP-tagged neuronal isoform, as an anti-DIC antibody recognizing both tagged DIC1 and the ubiquitously expressed DIC2 isoform showed a near identical localization (Figure 1D, analysis of axon tips gives a mean Pearson’s coefficient of 0.80 ± 0.03 ; $n = 18$ from 2 independent cultures).

To understand the dynamics of dynein-GFP accumulation, we performed fluorescence recovery after photobleaching (FRAP) experiments on growth cones at 8 DIV (Figure 1F). We found that distal dynein-GFP accumulations recovered very slowly after bleaching, indicating that cytoplasmic dynein does not undergo free diffusion. However, by comparing the distal bleached $5 \mu\text{m}$ to a more proximal axon region, we found that although absolute fluorescence intensity did not recover within 20 min, the relative enrichment of dynein distally compared to more proximal regions of the axon did recover (Figure 1F).

In these FRAP experiments, it was difficult to visualize individual transport events driving signal recovery. To improve our signal to noise, we imaged axonal dynein-GFP using near-total internal reflection fluorescence microscopy (near-TIRF). Axon kymographs were generated (Figures 1G and 1H) with anterograde and retrograde events appearing as diagonal lines angled right and left, respectively. These kymographs showed many short anterograde events of comparatively uniform velocity and low signal intensity. When we bleached regions of the axon and imaged recovery with near-TIRF, the same uniform velocity events were observed to move into the bleached area (Figure 1H). Typical anterograde events had a speed of $\sim 1 \mu\text{m/s}$, equivalent to the known speed of kinesin-1.

Figure 1. Dynein-GFP Accumulates in the Axon Terminals of Primary Hippocampal Neurons throughout Development

(A) Models for dynein transport in the axon: (i) carrying extra dynein motors on vesicles; (ii) recruitment and surfing of microtubule +TIPs; and (iii) direct transport by kinesin.

(B–E) Immunofluorescence and confocal microscopy of dynein-GFP primary hippocampal neurons. (B) Dynein-GFP accumulates in tau-positive axons at 8 DIV (small arrowheads), with particular enrichment in the axon terminals (empty arrowheads). Dynein-GFP accumulation does not colocalize with the presynaptic marker SV2 at 8 DIV (Figure S1A) or 21 DIV (C, empty arrowheads), or with the postsynaptic marker PSD-95 (Figure S1B). (D) Dynein-GFP is colocalized with anti-DIC (colocalization appears white, neuron shown at 12 DIV). (E) Dynein-GFP is colocalized with GAP43 at 3 DIV (filled arrowhead, GAP43-positive terminal; empty arrowhead, GAP43-negative terminal).

(F) FRAP analysis of dynein-GFP localization to axon terminals shows recovery of distally accumulated dynein takes >20 min (left). Quantification (right) shows ratio of the mean intensity of the distal $5 \mu\text{m}$, d, over the more proximal $5 \mu\text{m}$ region, p, $50 \mu\text{m}$ away.

(G) Left: first frame, kymograph, and last frame of a dynein-GFP hippocampal axon imaged using near-TIRF. Scale bar indicates anterograde direction. Middle: selected events highlighted for clarity. Right: enlargement of boxed region. Arrowheads point to start (empty) and end (filled) of selected anterograde events.

(H) Left: first frame, kymograph and last frame of a dynein-GFP hippocampal axon imaged by near-TIRF after bleaching. Scale bar indicates anterograde direction. Right: selected events highlighted for clarity.

Dynein Accumulates in Neurites Coincident with Axon Specification

As dynein-GFP is already accumulated in the growth cones of young (stage 3) neurons, we wondered whether dynein accumulated in the nascent axonal neurite prior to, or only after, axon specification. To answer this question, we carried out overnight live cell imaging of axon specification in developing stage 2 hippocampal neurons from dynein-GFP mice. Stage 2 development is characterized by the protrusion of several short neurites with plus-end out microtubule orientation (Baas et al., 1989). Upon axon specification in stage 3, one neurite undergoes a period of growth, simultaneously acquiring an axonal phenotype (Jacobson et al., 2006).

To our surprise, prior to axon specification the accumulation of dynein-GFP in any one neurite was highly dynamic and transient, with accumulation apparent in only one or two neurites at any given time (Figure 2A and Movie S1; filled arrow head indicates dynein accumulation). This behavior could be quantified by expressing the integrated density of dynein-GFP fluorescence in one neurite as a percentage of the total dynein-GFP signal in all neurites (Figures 2B and 2C). Transient accumulations of dynein moving from neurite to neurite were seen right up until the moment of axon specification, when dynein became enriched in the nascent axonal neurite coincident with the characteristic growth spurt (Figure 2C). Dynein accumulation persisted during extension of the axonal growth cone (Figure 2C and Movie S1). Although some dynein-GFP remains in the somato-dendritic compartment throughout development, we did not observe any further prominent accumulations in young dendrites during this time frame.

The behavior of dynein-GFP in this assay was strikingly reminiscent of observations on the transient and stochastic oscillation of the constitutively active tailless kinesin-1 construct, K560, among developing neurites (Jacobson et al., 2006). These oscillations are followed by the stable accumulation of K560 in a single neurite as one of the earliest markers of axonal identity, leading to the hypothesis that this selectivity ensures that kinesin-1 cargoes are targeted to just one neurite. Thus, we compared the dynamics of dynein and kinesin by expressing Halo-tagged K560 labeled with tetramethylrhodamine (TMR) in hippocampal neurons from the dynein-GFP mouse. Dynein-GFP and K560-Halo can be seen co-migrating among stage 2 neurites prior to axon specification (Movie S2 and Figures 2D and 2E). The co-migration of these two markers was not an artifact due to volume changes, as the cytosolic marker BFP did not show the same behavior (Figure S2 and Movie S3). When the integrated density of neurite fluorescence was quantified (Figure 2F), the movement of K560 among neurites was found to be faster and more complete than dynein-GFP, resulting in sharper, more defined peaks over time, although the same overall dynamics were observed. This difference likely reflects the fact that K560, lacking key regulatory domains and unbound from cargo, is free to rapidly respond to changes in the microtubule cytoskeleton, whereas dynein-GFP is part of an endogenous complex with multiple cellular roles to perform.

Dynein Intermediate Chain Interacts Directly with Kinesin-1

The co-migration of dynein-GFP and K560 in developing neurites suggests that there may be a kinesin-1-dependent mechanism

for the anterograde transport of dynein in the axon. Previous work from our lab identified a direct interaction between the neuron-specific DIC1 isoform of dynein and kinesin-1 (Ligon et al., 2004), raising the possibility that dynein complexes are directly transported by kinesin-1 in the axon. We set out to characterize the dynein-kinesin interaction in more detail to examine this possibility.

Endogenous kinesin-1 is a tetramer formed of two heavy chains (encoded by KIF5A, KIFB, or KIF5C) and two light chains (KLC1 and KLC2). We previously identified an interaction between DIC1 and KLC, with a strong preference for KLC2 over KLC1 in *in vitro* binding assays (Ligon et al., 2004). We confirmed these previous studies by overexpressing full-length proteins from COS cell lysates (Figure 3B) and found that 5-fold more KLC2 than KLC1 was co-immunoprecipitated with DIC1a in this assay (Figure 3C).

Tryptophan-based motifs mediate binding to the tetratricopeptide repeat (TPR) domains of KLCs (Dodding et al., 2011; Pernigo et al., 2013). DIC1 was identified in a bioinformatics search using a bipartite tryptophan motif consensus sequence (Dodding et al., 2011), and the location matched our previously reported KLC binding site on DIC1 (Ligon et al., 2004) (Figure 3A). These motifs (WD1 and WD2) lie within two short alternatively spliced sequences in DIC1 (AS loop 1 and AS loop 2, respectively, see Figure 3A and Figure S3) but are absent from the ubiquitously expressed isoform DIC2c (Kuta et al., 2010), thus only neuronal dynein is predicted to bind KLC using these motifs.

To probe the role of the tryptophan motifs, we tested the ability of peptides derived from the AS1 and AS2 loops to interact with purified KLC1 or KLC2 TPR domains using fluorescence polarization (Figures 3D and 3E). A TAMRA-conjugated 11-amino-acid-long peptide centered on the first tryptophan motif (WD1^{pept}) bound to KLC1^{TPR} with a K_D of $7.58 \pm 0.61 \mu\text{M}$ and to KLC2^{TPR} with a K_D of $9.18 \pm 0.26 \mu\text{M}$. These affinities are similar to those of peptides with tryptophan motifs from either the lysosomal cargo adaptor, SifA-kinesin interacting protein (SKIP), or Calsynenin-1 (Pernigo et al., 2013). In contrast, a peptide centered on the second tryptophan motif (WD2^{pept}) did not show an interaction in this assay, similar to the behavior of the second tryptophan motif within the SKIP protein (Pernigo et al., 2013). WD1^{pept} polarization was reduced in a concentration-dependent manner by titrating increasing amounts of unlabeled SKIP peptides, consistent with their binding being mutually exclusive, as they likely occupy the same topological location on KLC2^{TPR} (Figure S3D).

To examine the contribution of the tryptophan motifs to the DIC-KLC interaction in the context of full-length proteins, we tested the effect of alanine substitutions of either the tryptophan or the following aspartic acid residues of WD1 and WD2 on the ability of DIC1 to co-immunoprecipitate KLCs (Figures 3F–3I). Three mutants were examined: alanine mutation of WD1 (WD1AA), WD2 (WD2AA), and WD1 and 2 combined (WD1 and 2AA). For both KLC1 (Figures 3F and 3G) and KLC2 (Figures 3H and 3I), only the double mutant of both WD1 and 2 showed a consistent decrease in relative binding to KLC. Thus, although binding between the WD2 peptide and KLC^{TPR} was not detected *in vitro*, both motifs are important in the context of the full-length proteins.

An emerging commonality of active kinesin-1 transport complexes is the formation of multiple interactions between

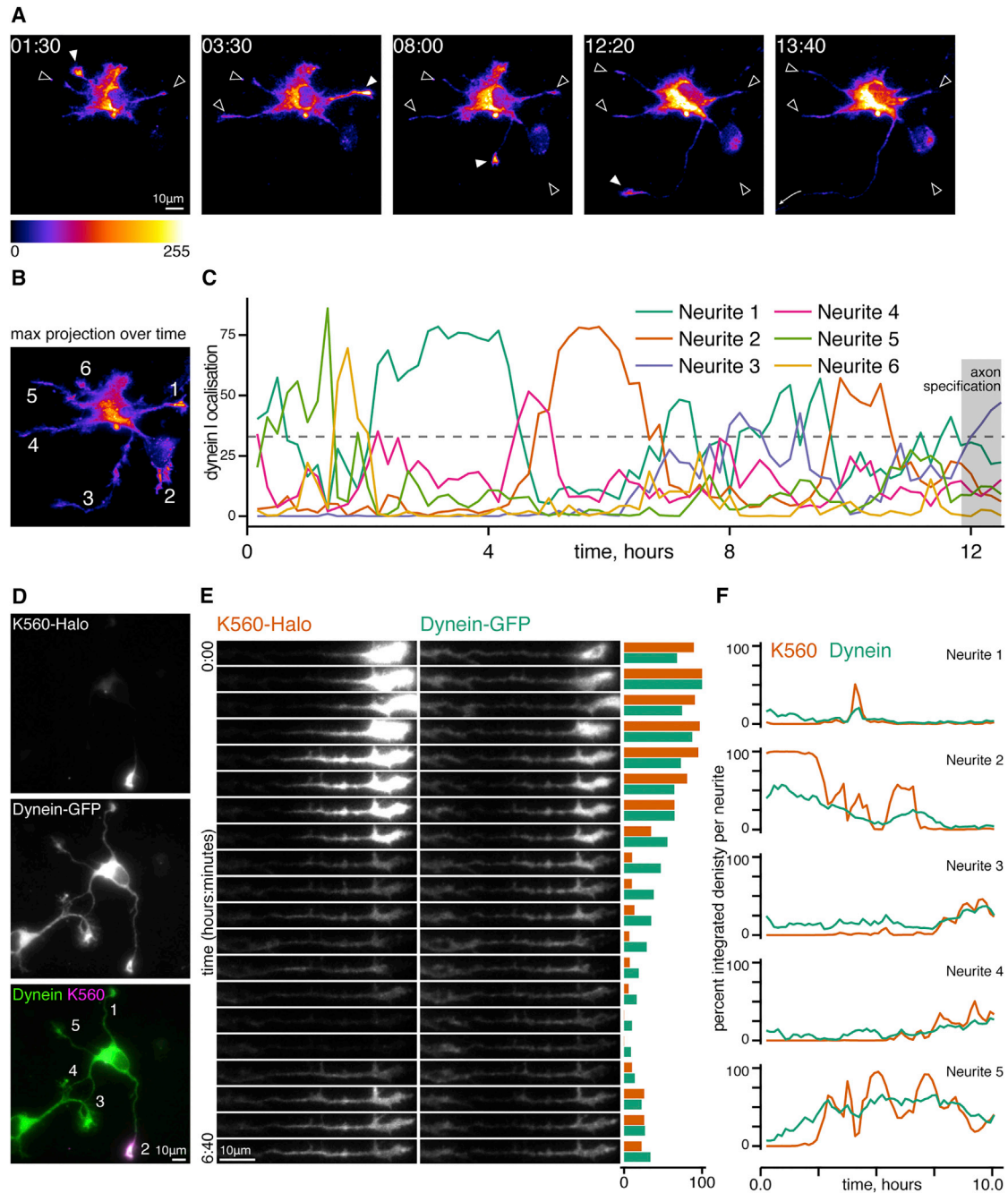


Figure 2. Dynein Accumulates in the Growth Cone Coincident with Axon Specification

(A) Still images from [Movie S1](#) showing neurite outgrowth in dynein-GFP stage 2 neuron. Filled arrowhead, neurite with highest dynein-GFP intensity; empty arrowheads, other neurites. Long arrow shows direction of axon exit. Time stamps, hours:minutes; fluorescence intensity scale, bottom left.

(B) Maximum projection of [Movie S1](#) with neurite labeling used in (C).

(C) Individual neurite integrated density as a percentage of the total in all neurites from [Movie S1](#) through time. Neurites labeled as in (B).

(D) Maximum projection of [Movie S2](#), dynein-GFP neuron transfected with K560-Halo, indicating neurite labeling for (E) and (F).

(E) Still images of Neurite 2 (see D) through time. Quantification bars show relative integrated density of K560 (orange) and dynein-GFP (green) within Neurite 2 over time.

(F) Individual neurite integrated density as a percentage of the total in all neurites from [Movie S2](#) through time. Neurites labeled as in (D). See also [Figure S2](#).

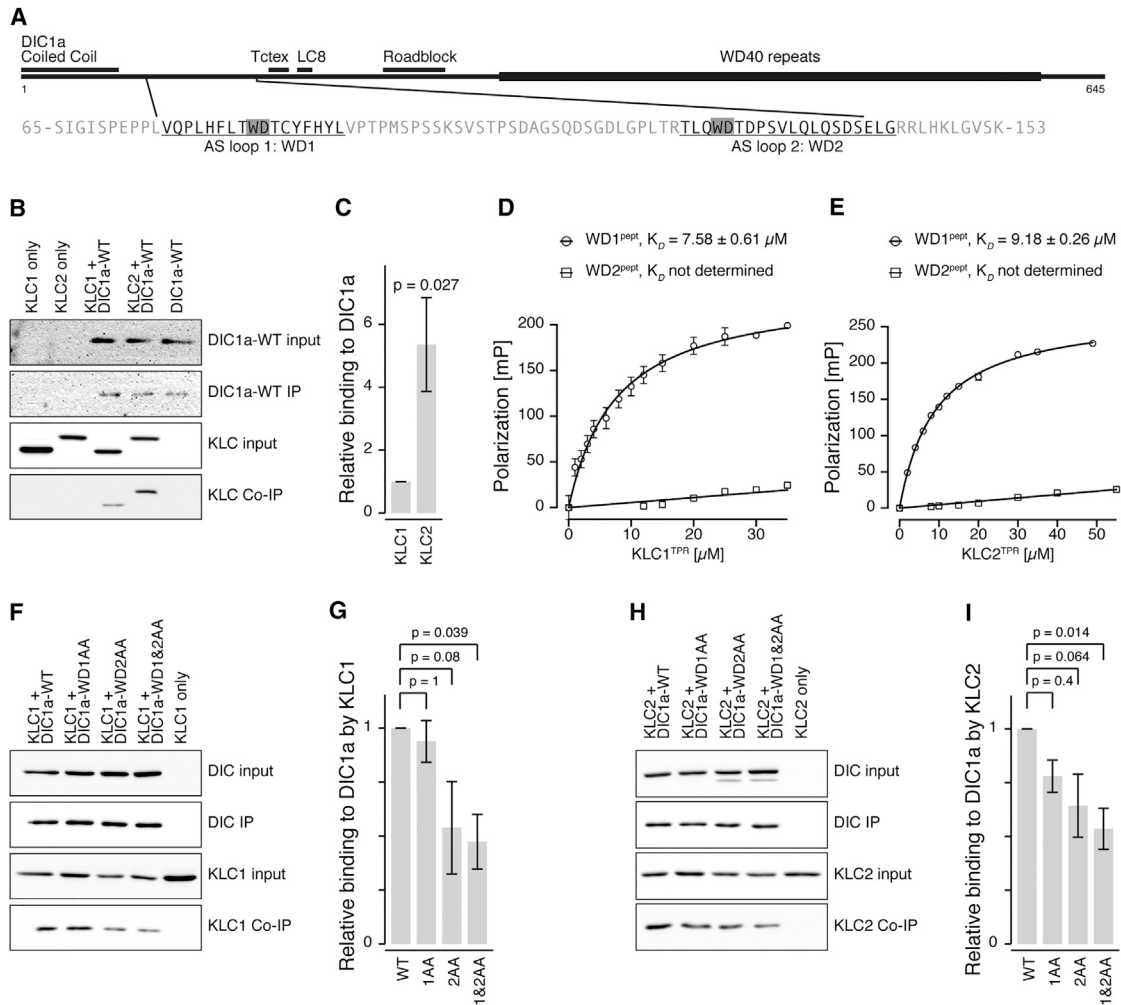


Figure 3. DIC1 Interacts Directly with KLCs through DIC1 Tryptophan Motif Binding to the KLC TPR Domains

(A) Schematic of DIC1 showing structural motifs and dynein light chain binding sites relative to the alternatively spliced regions (AS loops 1 and 2) and WD motifs (WD1 and WD2, in gray). See also Figure S3.

(B and C) COS cells cotransfected with mCherry-tagged DIC1a and HA-tagged KLC as indicated followed by immunoprecipitation (IP) with anti-mCherry (B, western blotting with anti-DIC and anti-HA). (C) Co-IP efficiency expressed as band intensity relative to KLC1 \pm SEM; $n = 4$ experiments.

(D and E) Fluorescence polarization measurements with peptides of the first and second DIC1 tryptophan motifs (WD1^{pept} and WD2^{pept}, respectively) binding to the TPR domain of KLC1 (D) and KLC2 (E). K_D values determined at 150 mM NaCl; error bars \pm SEM, experiments typically done in triplicate. See also Figure S3.

(F–I) COS cells cotransfected with mCherry-tagged DIC1a (wild-type, WT; or point mutations of WD1, WD2, or both WD1 and 2 to alanine, AA) and HA-tagged KLC1 (F) or KLC2 (H) as indicated followed by IP with anti-mCherry (F and H, western blotting with anti-DIC or anti-HA). (G and I) Co-IP efficiency expressed as band intensity relative to WT DIC1a \pm SEM; $n = 6$ and 4 experiments, respectively.

the motor and the cargo, including associations with both KLCs and the KIF5 heavy chain (KHC). For example, the cargo adaptor proteins HAP1, JIP1, and JIP3 all interact with both KIF5 and KLC (reviewed in Fu and Holzbaur, 2014). Consistent with this model, in a yeast two-hybrid screen for binding partners of DIC1a (Perlson et al., 2013), we identified residues 389–637 of KIF5A, a region conserved among all three KIF5 isoforms (57.4% and 62.2% identity with KIF5B and KIF5C, respectively). Consistently, immunoprecipitations with all three myc-tagged KIF5 isoforms co-precipitated DIC1a (Figure 4A). We further mapped the DIC1a interaction domain in immunoprecipitation experiments with KIF5C “head” (1–560), “stalk”

(561–774), and “tail” (775–956) constructs. DIC1a was co-precipitated with the stalk region of KIF5C, identifying a consensus binding region spanning residues 561–636 of KIF5C (Figures 4B and 4C). This region encompasses the central hinge region of KIF5 that allows the motor to fold to form an auto-inhibited conformation (Friedman and Vale, 1999; Hackney et al., 1992). Effector binding to this hinge region can stabilize the open conformation of kinesin-1 to create an active transport complex (Fu and Holzbaur, 2013).

In summary, interaction between DIC and kinesin-1 is mediated by neuron-specific isoforms of DIC, KLC TPR domains, and the stalk region of the KIF5 heavy chains. Together, these

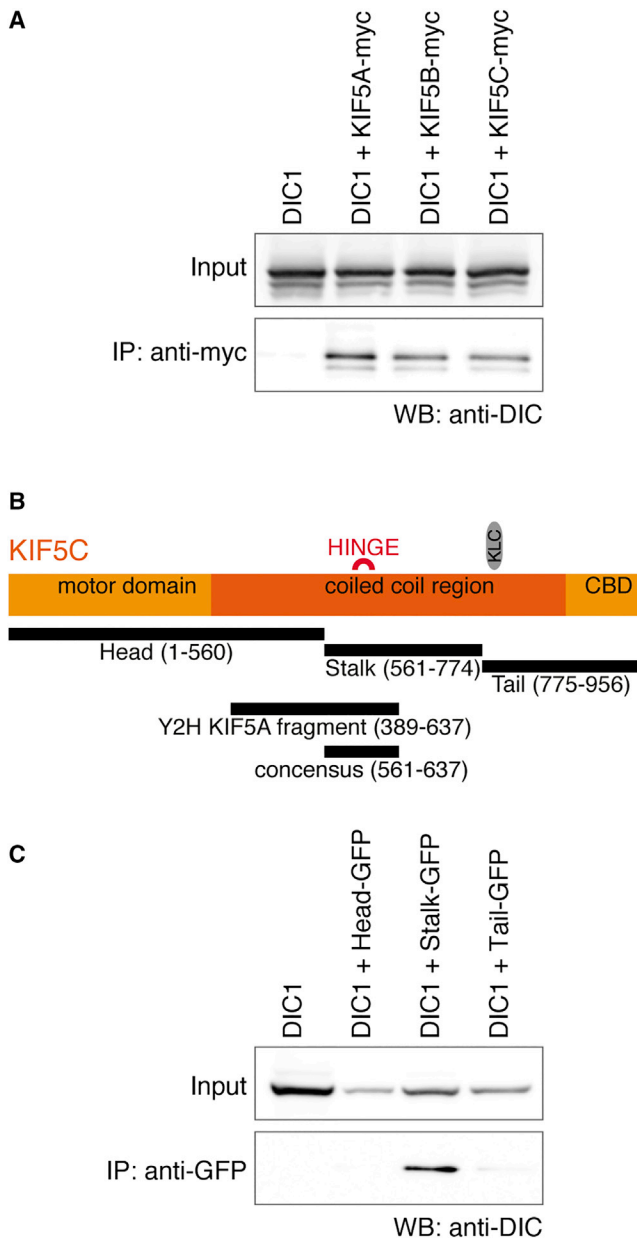


Figure 4. DIC1a Interacts with the Central Stalk Region of KIF5 Heavy Chains

(A) Western blot (WB) of COS cells cotransfected with mCherry-tagged DIC1a and myc-tagged KIF5A-C constructs as indicated followed by immunoprecipitation with anti-myc.

(B) Schematic of KIF5 showing the constructs used in (C), the sequence isolated by yeast two-hybrid screen and the resulting consensus region for binding DIC relative to key domains: motor domain, coiled-coil, cargo binding domain (CBD), central hinge, and KLC binding region.

(C) Western blot (WB) of COS cells cotransfected with mCherry-tagged DIC1a and GFP-tagged KIF5C “head,” “stalk,” and “tail” constructs shown in (B) followed by immunoprecipitation with anti-GFP.

interactions are likely to stabilize a dynein-kinesin complex capable of active transport.

An Endogenous Complex of Kinesin-1 and Cytoplasmic Dynein Is Found in Brain

Next, we asked whether dynein-kinesin complexes form in the brain. Cytosolic dynein can be enriched from a $100,000 \times g$ supernatant fraction from mammalian brain (Ayloo et al., 2014); dynein from this fraction is readily separated from kinesin using a sucrose gradient (see Figure S4A) and so an endogenous dynein:kinesin complex is unlikely to be found in this fraction. Instead, Scott et al. proposed that after differential centrifugation of homogenized brain, the synaptosome-depleted (S2) fraction could be reasonably assumed to contain the majority of material that is moved within axons (Scott et al., 2011), including soluble cytosolic proteins, small vesicles, and macromolecular protein complexes. These three phases can be further separated into a soluble cytosolic protein fraction (S3) and the remaining pellet (P3) with a $100,000 \times g$ spin. Resuspension of P3 and bottom loading onto a sucrose gradient yields floating small vesicles (V) separated from macro protein complexes (PC), which remain within high-density fractions at the bottom of the gradient. Following this procedure, Scott and colleagues found that a substantial fraction of the cytosolic proteins CaMKII and synapsin, known to travel by slow axonal transport, were found in association with both floating vesicles and the large protein complexes at the bottom of the gradient. Based on these observations, we sought to isolate an endogenous non-vesicular dynein:kinesin complex that may be responsible for the slow transport of dynein.

Brain homogenate from dynein-GFP mice was fractionated following the scheme in Figure 5A. Samples from fractions S1-P3 were adjusted to $1 \mu\text{g}/\mu\text{L}$ prior to SDS-PAGE and western blotting (Figure 5B). We compared the distribution of proteins between the cytosolic fraction (S3) and the P3 fraction that is enriched in small vesicles and macromolecules (Figure 5C). As expected, the vesicular marker GAP43 was largely concentrated in the vesicle-containing P3 pellet, as was the slow axonal protein synapsin. All dynein/dynactin subunits assessed had a similar distribution between the cytosolic S3 pool versus the vesicular/protein P3 pool (DHC, $38.2\% \pm 10.95\%$; DIC1, $20.4\% \pm 10.2\%$; DIC2, $22.2\% \pm 10.8\%$; p150, $25.1\% \pm 13.4\%$ present in S3). The kinesin-1 heavy chain, KIF5, had a slightly higher proportion present in the cytosol than dynein/dynactin ($46.6\% \pm 7.3\%$ in S3 versus a mean of 26.5% for all dynein/dynactin subunits); however, a key difference was in the relative distributions of KLC1 and KLC2. $85.9\% \pm 10.0\%$ of KLC2 was found in P3, compared to only $34.7\% \pm 18.8\%$ of KLC1. The relative enrichment of KLC2 in P3 suggests a key functional difference between KLC1 and KLC2 in brain.

To separate vesicles from protein complexes within P3, we bottom loaded the resuspended pellet onto a 15% – 45% sucrose gradient so that vesicles could be separated by their lower density (Figures 5D and 5E). Equal volumes of the 24 gradient fractions were used for SDS-PAGE and western blotting (Figure 5D). Protein concentrations from each fraction were assessed by absorbance at 280 nm and the vesicle distribution through the

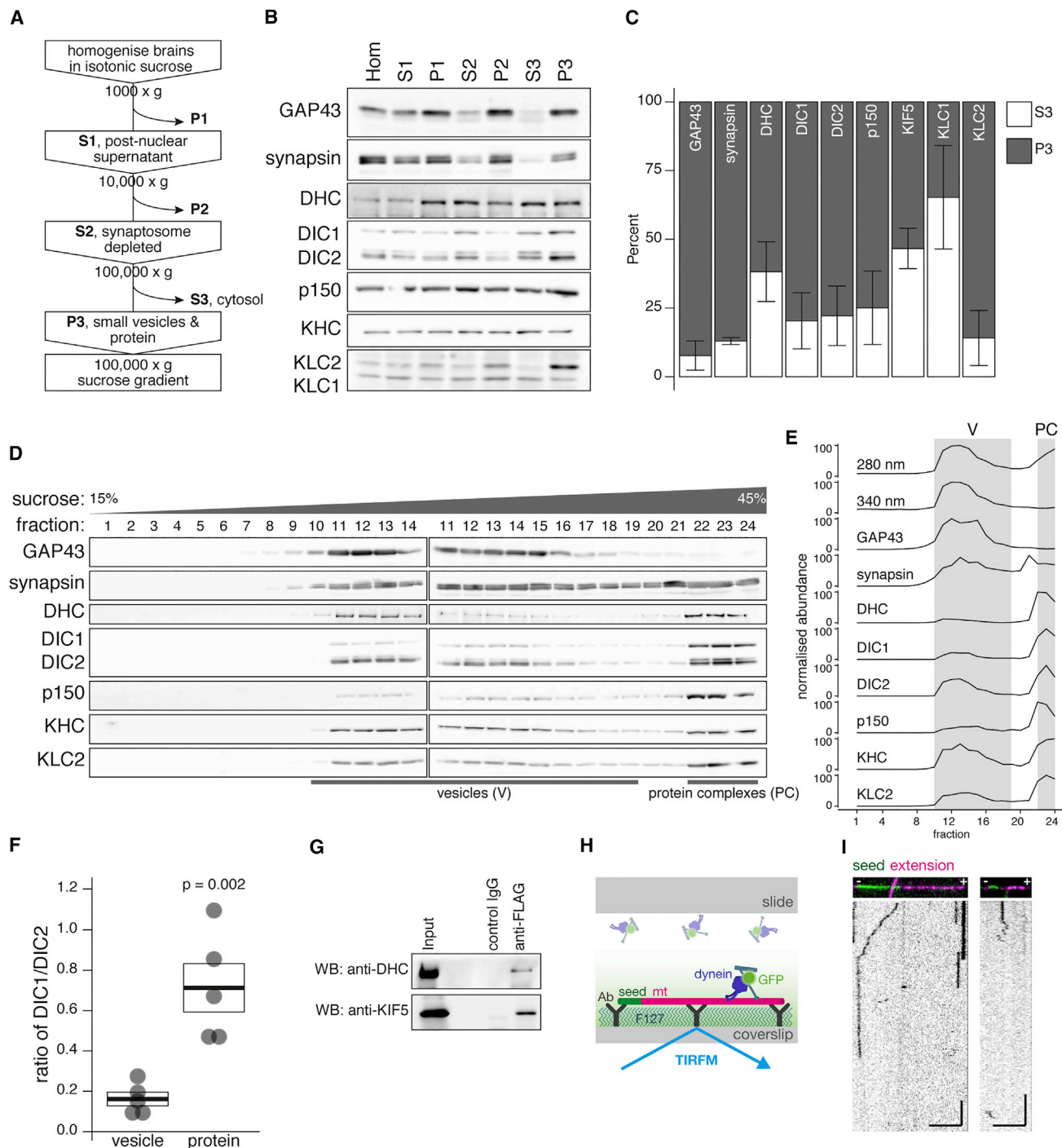


Figure 5. Biochemical Analysis of Endogenous Dynein-GFP and Kinesin Complexes from Brain

(A) Experimental procedure for dynein-GFP mouse brain differential centrifugation.

(B) Distribution of proteins of interest across centrifugation steps outlined in (A) by SDS-PAGE and western blotting. Antibodies for: vesicular marker GAP-43; slow transport marker synapsin; and motor protein subunits DHC, DIC, p150, KHC, and KLC.

(C) Quantification of the relative abundance of each protein in fractions S3 versus P3. $n = 3$; error bars \pm SEM.

(D) Distribution of proteins of interest across the 24 fractions of the P3 sucrose density gradient, showing separation of vesicles (V, fractions 10–19) from high-density protein complexes (PC, fractions 22–24). Protein association with vesicles was attenuated by the addition of Triton X-100 to the resuspended P3 fraction (Figure S4). Fractions 11–14 were loaded in duplicate to normalize band intensities across the two gels required to run all fractions.

(E) Quantification of the gradient assay in (D) highlighting the vesicular (V) and high-density protein fractions (PC).

(legend continued on next page)

fractions was assessed by turbidity at 340 nm (Figure 5E). The vesicle marker GAP43 showed clear separation from the bottom of the gradient and good agreement with the turbidity measurement of the samples, indicating that the majority of vesicles floated between fractions 10 to 19 (marked as “V” in Figure 5E). Measurements of absorbance at 280 nm showed a sharp rise in protein concentration between fractions 21 and 22; thus, fractions 22–24 were designated as the high-density protein fractions (“PC” in Figure 5E). There was relatively more protein associated with the “V” fractions compared to “PC” fractions. All motor subunits assessed had distinct vesicle- and protein-associated pools, and in fact showed a substantial enrichment in the densest fractions relative to the total protein distribution. An intriguing difference was in the distribution of DIC isoforms 1 and 2 between vesicles and dense protein fractions. In the dynein-GFP mice, DIC1 is separated from DIC2 by the molecular weight of the exogenous GFP tag; using the anti-DIC antibody to detect both isoforms we directly compared the ratio of DIC1 to DIC2 from band intensities (Figure 5F). The ratio of DIC1/DIC2 in the vesicular fraction was 0.16 ± 0.03 , whereas in the protein fraction the DIC1/DIC2 ratio was 0.71 ± 0.1 , a 4.4-fold increase. This finding demonstrates isoform specificity between the pools of dynein and is consistent with the relative enrichment of both DIC1 and KLC2 in the PC fraction.

To isolate a possible non-vesicular dynein:kinesin complex, we carried out immunoprecipitation of dynein from the high-density fractions 23–24, using antibodies to the 3xFLAG tag knocked into the DIC1 C terminus. Using this strategy, we coprecipitated dynein heavy chain and kinesin heavy chain using anti-FLAG antibody (Figure 5G).

Next, we asked whether the protein in high-density fractions of the sucrose gradient was functional—that is, whether it represents native macromolecular complexes or alternatively is comprised of protein aggregates precipitated during fractionation. We analyzed the protein fraction by single molecule TIRF microscopy using polarity marked microtubules (Figure 5H). GFP puncta bound to microtubules (Figure 5I) and we observed both minus-end-directed (left) and plus-end-directed (right) motility. While the extent of binding and motility from prep to prep was highly variable, likely due to the dilute nature of the protein fractions, qualitatively the events observed differed from the motility of either purified dynein or dynein-associated vesicles, as fewer directional switches were observed (Hendricks et al., 2010; Ross et al., 2006). Plus-end-directed motility in this assay is consistent with the anterograde bias of slow transport observed in cells; the minus-end-directed motility that was also observed may represent partial activation of dynein activity under the conditions of the assay, for example, by loss through dilution of a negative inhibitor such as Lis1.

Anterograde Bias in Dynein Transport Can Be Directly Observed

As noted above, there is a persistent anterograde bias in dynein transport throughout development, leading to accumulation in the peripheral axon and growth cone (Figure 1). Such an accumulation, which is the reverse of what would be expected to result from a passive diffusion from the site of synthesis, requires active transport in the anterograde direction. Recent success in imaging slow axonal transport of cytosolic proteins used photoactivation to create a discrete pool of protein that could be tracked in real time (Scott et al., 2011). We modified this assay in two ways. First, we used photobleaching to establish a discrete photo-protected population of dynein-GFP, expressed at endogenous levels in neurons, flanked by bleached areas allowing us to monitor movement along the axon. Second, we developed a new quantification method to track the midpoint of the photo-protected pool through time (Figure 6).

Primary hippocampal neurons from dynein-GFP mice were cultured for 8–10 DIV in 900 μm microfluidic devices in order to image single axons of known polarity. Post bleach motility was imaged for 60 s at 0.5 fps. A line scan was made for every frame of the time series, then movement of the photo-protected dynein-GFP pool was quantified by defining retrograde and anterograde edges at the half-maximal fluorescence value and tracking the displacement of the midpoint (Figure 6B). The peak of fluorescence intensity decreased with time as the dynein-GFP pool shifted in both anterograde and retrograde directions. However, the relative midpoint could be seen moving with a clear bias in the anterograde direction for several seconds (Figure 6C), particularly when overlaid onto the more standard kymograph representation of axonal transport (Figure 6D). Plotting the mean \pm SEM of several axonal dynein-GFP displacements reveals a net anterograde bias of $\sim 1\text{--}2 \mu\text{m}/\text{min}$ (Figure 6E). By fitting a linear regression to each relative midpoint position over time, we observed anterograde velocities ranging from 0.01 to 0.1 $\mu\text{m}/\text{s}$. However, $\sim 80\%$ of events were in the 0.01 to 0.05 $\mu\text{m}/\text{s}$ range or approximately 1–5 mm a day. All net anterograde velocities were consistent with known speeds of slow axonal transport of cytoplasmic dynein in vivo (Dillman et al., 1996a, 1996b).

Anterograde Transport of Dynein Is Dependent on Microtubules and Interaction with the KLC TPR Domain

So far, we have established that cytoplasmic dynein moves with an anterograde bias along axons of developing hippocampal neurons, resulting in a distal accumulation following axon specification. Further, a dynein-kinesin-1 complex can be biochemically isolated from a non-vesicular fraction of brain. To directly test whether dynein is transported down the axon by kinesin, we utilized our axonal transport photobleaching assay.

(F) The ratio of DIC1 to DIC2 in vesicle fractions from the gradient assay compared to high-density protein fractions. $n = 5$ (gray circles), mean ratio (heavy line) \pm SEM (box) is shown.

(G) KIF5 and DHC co-immunoprecipitate in an endogenous complex from fractions 23 and 24 (D) with anti-FLAG.

(H) Schematic of experimental set up for (I). Rhodamine-labeled microtubules were extended from AMCA-labeled microtubule seeds to indicate polarity, then immobilized onto silanized coverslips by anti-tubulin antibody. Dynein-GFP events were imaged by TIRF microscopy (TIRFM).

(I) Two polarity-marked microtubules and example kymographs of dynein-GFP events on those microtubules imaged by TIRFM. Vertical scale is 10 s; horizontal scale is 5 μm .

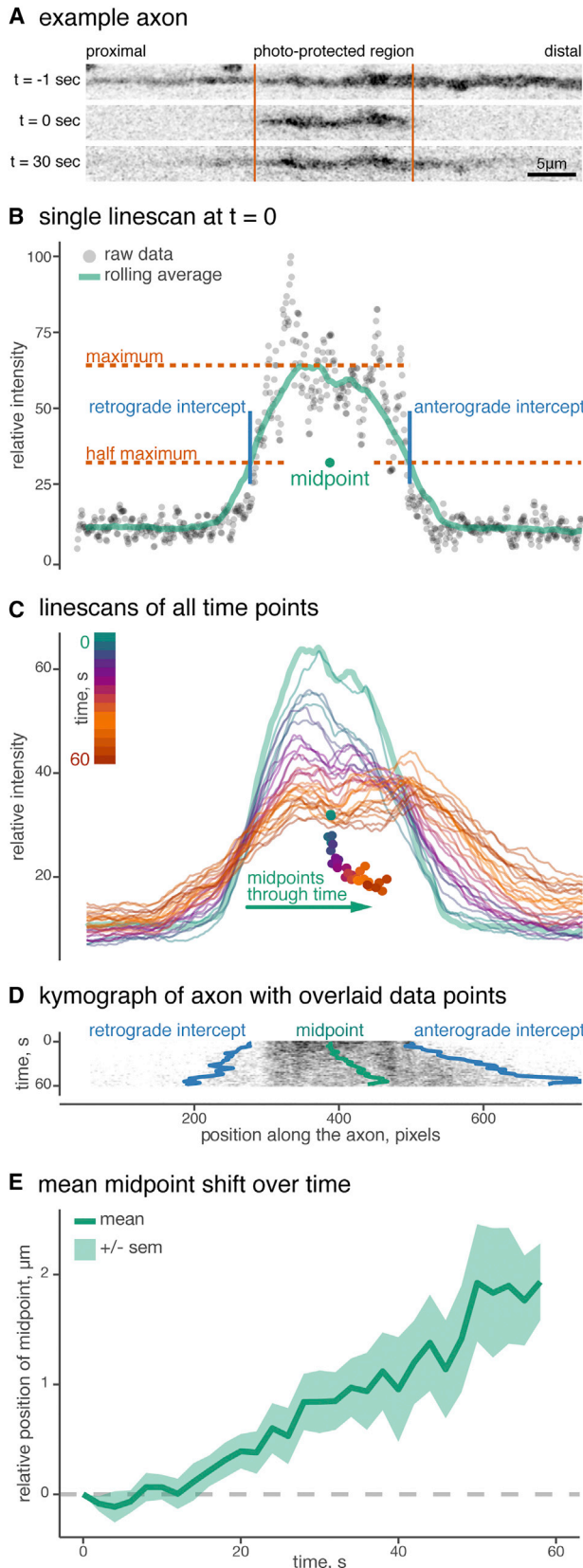


Figure 6. Discrete Populations of Dynein-GFP Move with an Anterograde Bias in the Axon

(A) Example axon before ($t = -1$) and after ($t = 0$) bleaching. The relative position of the soma is indicated.

(B) Midpoint calculation of dynein-GFP photo-protected region for $t = 0$. The relative intensity of the axon line scan at $t = 0$, showing raw data (gray dots) and rolling average (green line). Anterograde and retrograde fronts of the photo-protected population are defined as the positions along the axon where the intensity is half-maximal. The midpoint is defined as halfway between these two intercepts.

(C) Line scans and midpoints for all time points of the movie, demonstrating a displacement toward the distal axon with time. Color changes with time indicated by the scale bar, top left.

(D) Kymograph of dynein-GFP axon from (A) showing anterograde movement of the photo-protected region, over plotted with the calculated midpoints and intercepts from (C).

(E) The mean displacement of the midpoint through time (green line) from $n = 11$ neurons, \pm SEM (green ribbon).

First, we tested whether the anterograde transport of dynein was microtubule dependent, using nocodazole (final concentration $30 \mu\text{M}$) to depolymerize microtubules. Every viable isolated axon (see [Experimental Procedures](#)) within the microgrooves of the chamber was imaged following the bleaching protocol described above. The relative position of the midpoint for each kymograph was calculated (see [Figure 7A](#) for examples) and the mean midpoint displacement \pm SEM was plotted for all axons ([Figure 7B](#)). Nocodazole treatment abrogated the anterograde bias in transport seen in DMSO control neurons, with no net motility in either the anterograde or retrograde direction. To establish a mean velocity for dynein-GFP, we fitted each midpoint shift with a linear regression. In the DMSO control, dynein-GFP had a mean velocity of $0.018 \pm 0.005 \mu\text{m/s}$, whereas nocodazole treatment reduced this to $-0.001 \pm 0.005 \mu\text{m/s}$ ([Figure 7C](#)).

Axonal microtubules are uniformly orientated with polymerizing plus ends moving away from the soma. Dynein can be recruited to microtubule plus ends via dynactin and the +TIPs EB1 and CLIP-170 ([Moughamian et al., 2013](#)). Dynein surfing via +TIPs could be an alternative microtubule-dependent hypothesis for the anterograde transport of dynein in the axon ([Figure 1A](#)). We tested this by using taxol to stabilize microtubules and inhibit the formation of microtubule comets in the axon ([Figure S5A](#)). Taxol-treated axons showed no inhibition in the anterograde bias of dynein transport ([Figures S5B–S5D](#)). Of note, EB3 comets had a speed of $0.113 \pm 0.002 \mu\text{m/s}$ ($n = 399$, \pm SEM), which is ~ 10 -fold slower than the anterograde dynein events that we observed by near-TIRF imaging ([Figures 1G](#) and [1H](#)).

To directly test our hypothesis that interactions between dynein and kinesin-1 are required for the anterograde transport of dynein in the axon, we designed a peptide to block the interaction between DIC1 and KLC. We chose a 19-amino-acid-long sequence centered on the tryptophan in WD1 of DIC1a. This incorporated the alternatively spliced region AS loop 1, the region that we demonstrated interacted directly with the TPR of KLC using *in vitro* binding assays ([Figures 3D](#) and [3E](#)). The control peptide also had a central tryptophan residue, but the upstream and downstream sequences were scrambled, maintaining overall charge and residue composition ([Figure 7D](#)).

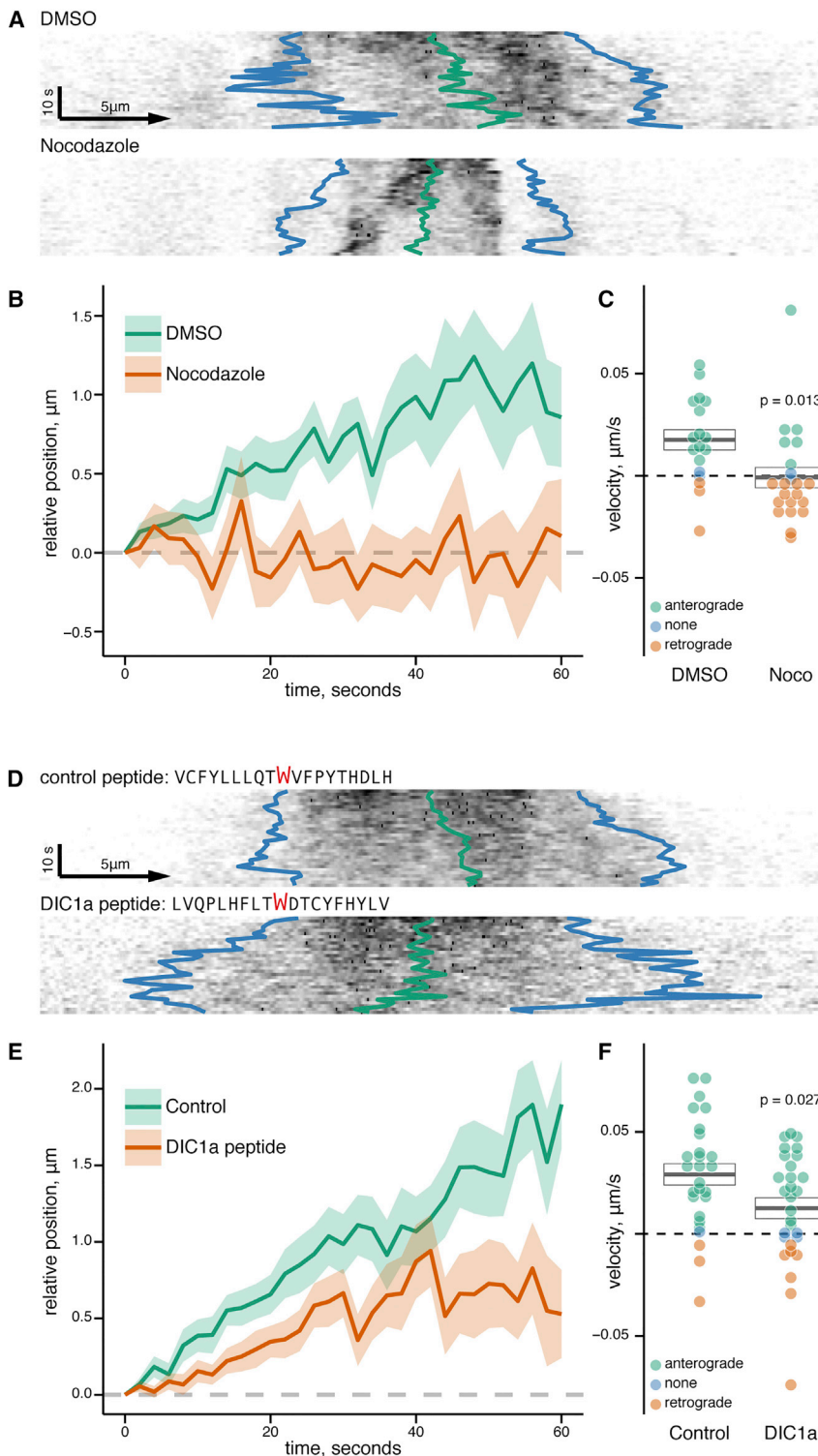


Figure 7. Slow Anterograde Transport of Dynein in the Axon Is Dependent on Microtubules and an Interaction with Kinesin

(A) Kymographs of DMSO control and nocodazole-treated axons from dynein-GFP hippocampal neurons showing relative positions of anterograde and retrograde intercepts (blue) and the calculated midpoint displacement (green). Scale bar indicates anterograde direction.

(B) The mean relative position of the midpoint with time for DMSO and nocodazole-treated axons: $n = 18$ and 22 axons, respectively, from three independent primary cultures; solid lines, mean; ribbons, \pm SEM.

(C) A linear regression was fitted to each axon's midpoint displacement to find the velocity of displacement. The mean velocity (heavy line) \pm SEM (box) is shown. Overlaid spots are the velocities for each measured kymograph with colors indicating overall direction of the kymograph.

(D) Kymographs of control and DIC1a peptide-treated axons from dynein-GFP hippocampal neurons showing relative positions of anterograde and retrograde intercepts (blue) and the calculated midpoint displacement (green).

(E) The mean relative position of the midpoint with time for control and DIC1a peptide-treated axons: $n = 27$ and 29 axons respectively from 3 independent primary cultures; solid lines, mean; ribbons, \pm SEM.

(F) Results of linear regression on each axon's midpoint displacement to find the velocity of displacement. The mean velocity (heavy line) \pm SEM (box) is shown. Overlaid spots are the velocities for each measured kymograph with colors indicating the overall direction of the kymograph.

DIC1-peptide-treated axons had a substantial reduction in the anterograde bias of dynein-GFP transport (Figure 7E). All dynein-GFP population velocities calculated by linear regression of individual midpoint shifts are shown in Figure 7F. In the presence of the control peptide, dynein-GFP had a mean velocity of $0.029 \pm 0.005 \mu\text{m/s}$, whereas the presence of DIC1a peptide reduced this by over 50% to $0.012 \pm 0.005 \mu\text{m/s}$. This reduction in mean velocity was accompanied by a more than doubling of the number of kymographs with no net direction bias or retrograde bias in the presence of DIC1a peptide (38% showed no or retrograde bias in DIC1a peptide experiments versus 15% in control experiments), as well as a complete loss of kymographs showing anterograde velocities over $0.05 \mu\text{m/s}$

Hippocampal neuronal cultures were pre-treated for 45–60 min with either DIC1a or control peptide, complexed with Chariot reagent for delivery across the plasma membrane. Using our photobleaching protocol followed by analysis of midpoint displacement through time for each kymograph, we found that

kymographs showing anterograde velocities over $0.05 \mu\text{m/s}$ (22% of control kymographs had a velocity over $0.05 \mu\text{m/s}$; mean velocity of anterograde only kymographs was $0.036 \pm 0.004 \mu\text{m/s}$ and $0.029 \pm 0.003 \mu\text{m/s}$ for control and DIC1a peptides, respectively). Consequently, the anterograde transport of

dynein-GFP in the axon is critically dependent on the interaction between dynein subunit DIC1a and the KLCs of kinesin-1.

DISCUSSION

Slow axonal transport is a well-established phenomenon *in vivo* thanks to extensive pulse chase labeling experiments in vertebrate nerves since the 1960s (reviewed recently in Roy, 2014). However, the underlying mechanisms driving this bulk transport phenomenon, and in particular the transport of non-cytoskeletal elements, are not well understood.

We have identified a non-vesicular complex of kinesin and dynein in the brain, which we show is responsible for the anterograde bias of dynein transport in the axon. This anterograde transport produces a net population velocity equivalent to those measured for SCb proteins *in vivo*. The complex is formed by direct interactions between the dynein intermediate chain and kinesin-1 heavy and light chains. Crucially, the KLC interaction is only seen with the neuron-specific isoform of DIC, DIC1, which preferentially binds KLC2 over KLC1 via paired WD motifs. Cellular fractionation experiments indicate that KLC2 is enriched in the high-speed pellet (P3) relative to KLC1, and DIC1 is enriched in non-vesicular sucrose fractions relative to DIC2. This demonstrates that dynein and kinesin are tailored to specific functions by their complement of accessory proteins. From our biochemical analysis, the majority of dynein is not associated with vesicles, which fits well with *in vivo* data on the axonal transport of dynein showing that 80% moves by slow axonal transport in the SCb fraction, with just 15% associated with vesicles (Dillman et al., 1996b).

A key difference between our study and previous radio labeling studies (Dillman et al., 1996a, 1996b) is that our slow transport imaging analysis captures the total pool of labeled dynein, not just newly synthesized proteins. Observations on this total pool of dynein indicate that the flux of anterograde slow transport exceeds the opposing flux resulting from dynein-mediated retrograde trafficking events, thus leading to a net accumulation of dynein in the distal axon far from the site of synthesis (Figure 1) and essentially reversing the concentration gradient that would result by diffusion. While the relative balance of anterograde and retrograde trafficking may potentially shift in adults, producing slower transport rates and thus less pronounced distal dynein accumulation, *in vivo* data from adult nerves (Dillman et al., 1996a, 1996b) demonstrate that slow axonal transport persists into adulthood.

Cytoplasmic Dynein Is Dependent on Kinesin-1 Transport for Localization

Genetic perturbations in model organisms have previously suggested that the localization of dynein in cells is dependent on kinesin-1. For example, *Drosophila Khc* mutants show impaired retrograde transport of mitochondria in axons (Pilling et al., 2006). Similarly, the polar localizations of dynein and kinesin are co-dependent during the establishment of motor-dependent asymmetric mRNA localization early in *Drosophila* oogenesis, where recent work found that posterior localization of dynein could be rescued in *Khc* null oocytes by expression of a KIF5 construct lacking the C-terminal cargo binding tail region (the

last 125 amino acids), but not a shorter construct lacking the KLC binding region (Williams et al., 2014). These genetic data are in good agreement with our biochemical data on the DIC interaction with KIF5, where we found an interaction with the stalk region of KIF5, but not the C-terminal tail. In a proof-of-principle experiment, a minimal complex for dynein transport by kinesin was reconstituted from yeast proteins (Roberts et al., 2014), using a truncated dynein heavy chain, Kip2 (a member of the kinesin-7 family), and the yeast orthologs for EB1, CLIP-170 and Lis1. However, this complex is unlikely to play a role in neurons; the closest equivalent to Kip2 is the centromere-associated motor CENP-E, which is specialized to perform chromosome alignment in mitosis and is not known to have a role in axonal transport.

Filamentous fungi are excellent model organisms for the study of microtubule transport as they are both genetically tractable and their long hyphal compartments are axon-like with uniformly orientated plus ends out microtubules (Egan et al., 2012a). In *Aspergillus nidulans*, loss-of-function mutants demonstrate a cooperative role for dynein and dynactin in their plus-end localization to the hyphal tip, localization that is also dependent on the KIF5 ortholog, KINA (Zhang et al., 2003). This kinesin-1-dependent localization of dynein and dynactin in distal hyphae also occurs in *Ustilago maydis* (Lenz et al., 2006). Although not directly addressed in our study, the accumulation of dynactin in axon terminals of both *Drosophila* and mice is also known to be kinesin-1 dependent (Lloyd et al., 2012; Moughamian and Holzbaur, 2012). As a frequent binding partner of dynein, dynactin may also be part of the anterograde transport complex that we have described. In fact, it appears that the basic dynein:kinesin complex may be conserved across species, while additional neuron-specific interactions between DIC and KLC may enhance association to the levels required for a significant accumulation by axonal transport.

There are two mechanisms of targeting dynein to microtubule plus tips: (1) vectorial delivery along microtubules, and (2) direct recruitment to the plus tip from the cytosol. In large polarized cells, these represent two distinct necessities—first, the need to concentrate dynein distally so that, second, this enhanced local concentration can be used to facilitate a plus-end-specific loading mechanism. Creating a distinction between these two mechanisms is important as the molecules that direct kinesin-dependent vectorial movement of dynein in yeast (EB1, CLIP-170, and Lis1) are similar to those that direct the ordered recruitment of dynein to the plus tips of microtubules in mammalian systems (EB1, CLIP-170, and dynactin) (Moughamian et al., 2013; Nirschl et al., 2016). We used low-dose taxol to show that the vectorial movement of dynein in the axon is not dependent on dynamic microtubule plus tips and the direct recruitment pathway. In both fungi and neurons, Lis1 acts as an initiation factor for dynein-driven organelle transport and is required for dynein to leave the microtubule plus tip (Egan et al., 2012b; Lenz et al., 2006; Moughamian et al., 2013; Zhang et al., 2003). Thus, in axons we propose the following sequence of events: (1) the kinesin-1-mediated vectorial delivery of dynein; (2) followed by direct recruitment of dynein to the distal microtubule plus tips by EB1, CLIP-170, and dynactin (Nirschl et al., 2016); and (3) the initiation of retrograde transport aided by Lis1.

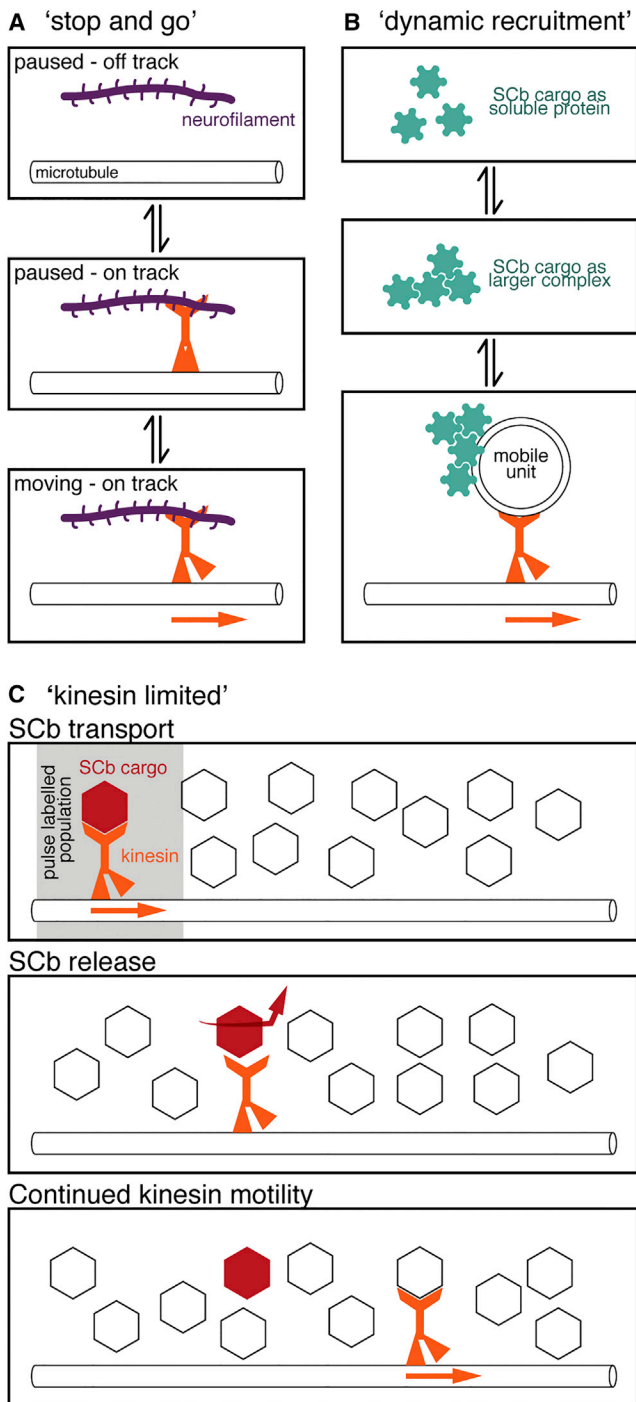


Figure 8. Different Mechanistic Models of Slow Axonal Transport

(A) The “stop and go” model describes the transport of neurofilaments in SCa. Through direct association with motors, neurofilaments switch between “off-track” and “on-track” states and between paused and motile states while “on-track” (Brown et al., 2005; Trivedi et al., 2007).

(B) The “dynamic recruitment” model describes the transport of some soluble cytosolic proteins moving in SCb, e.g., synapsin I (Tang et al., 2013). Soluble proteins come together to form larger complexes, which stochastically associate with vesicles (the mobile unit) undergoing transport.

In an alternative model based on an overexpression study in DRG neurons, the observation of co-transport of Lis1, DIC1, and TUBB3 led to the proposal that dynein is transported anterogradely in the axon through the Lis1-dependent immobilization of dynein on short “transport” microtubules (Yamada et al., 2008). However, tubulins are known to travel at SCa rather than SCb velocities (Grafstein et al., 1970; Hoffman and Lasek, 1975) and so this model is at odds with in vivo data showing that 95% of dynein is either moving in SCb or with vesicles (Dillman et al., 1996b). Thus, the tubulin co-transport model is unlikely to be sufficient to explain the pronounced distal localization of dynein that we have observed. Instead, the observed co-transport of dynein and tubulin may reflect a role for dynein in the active transport of microtubules along the axon (He et al., 2005).

The “Kinesin-Limited” Model of Slow Axonal Transport

There are currently two models describing slow axonal transport. The “stop and go” model describes the transport of assembled neurofilaments in SCa (Figure 8A) (Brown et al., 2005). Analysis of axonal neurofilament transport shows that neurofilaments cycle between two kinetic states termed “on-track” and “off-track” (Trivedi et al., 2007). On-track neurofilaments display short bouts of movement interrupted by short pauses, while off-track neurofilaments pause for much longer periods. Neurofilaments spend most of their time in the off-track state, producing overall very slow rates of transport. Neurofilaments rely on KIF5A and dynein for transport as assembled polymers, explaining why neurofilament instantaneous velocities are the same as those of fast axonal transport (Uchida et al., 2009; Wagner et al., 2004; Xia et al., 2003), although there are few molecular details about how motors are recruited to neurofilament polymers and why transport is sporadic. The “dynamic recruitment” model of slow axonal transport describes a mechanism in which SCb proteins can traverse the axon via transient formation of larger protein complexes and subsequent recruitment to vesicles for transport (Figure 8B) (Scott et al., 2011; Tang et al., 2013). This model is epitomized by the SCb cargo synapsin I, which has a high affinity for membranes. However, it is difficult to extrapolate this specific behavior to all other cytosolic proteins moving within SCb, as not all proteins have high affinity for membranes.

The coherent transport of numerous SCb proteins in the single peak observed in radiolabelling studies resulted in the hypothesis of a single carrier for SCb (Garner and Lasek, 1982). In truth, there are over 200 (mostly uncharacterized) proteins in SCb and it may be that one transport mechanism will not describe how all proteins are conveyed. The apparent coherence may mask a myriad of different mechanisms due to the limited spatio-temporal resolution possible with this approach.

(C) The “kinesin-limited” model also describes the transport of soluble cytosolic proteins moving in SCb. SCb cargoes such as dynein can directly associate with kinesin for short bursts of motility. By combining a limited ability to hold kinesin in an active state with a relatively low supply of active kinesin motors, slow transport cargoes would move much more slowly relative to kinesin due to the constant binding and release of cargo producing short bursts of motility.

The neurofilaments of SCa (Uchida et al., 2009) and now dynein in SCb both rely directly on kinesin-1. However, this remains the biggest conundrum: in order to produce such different transport rates, how is the recruitment and activation of kinesin different for slow transport cargos relative to fast vesicle transport? Based on our data demonstrating direct interactions between kinesin and the SCb cargo dynein, we present a third model for slow axonal transport, the “kinesin-limited” model (see below and Figure 8C).

Our model is based on two additional observations. First, a single kinesin has typical run lengths of just a few μm (Friedman and Vale, 1999). Kinesin recruitment to SCb cargo must be less stable than it is to vesicles (as otherwise SCb would have overall transport rates more similar to vesicles), and unstable kinesin recruitment would result in short spontaneous runs followed by dissociation from the microtubule track and disassembly of the transport complex. Second, only a very small percentage of kinesin-1 is observed to be traveling at SCb and SCa velocities in vivo (Elluru et al., 1995). Given the large volumes of protein moved by slow transport relative to fast transport, it is highly likely that there is a limited supply of activated kinesin motors in the axon. If a given SCb cargo loses its bound kinesin, this would naturally lead to long off-track times for SCb cargos and thus an overall net slow transport rate for that cargo. In contrast, the kinesin motor itself would continue to move down the axon in association with a new cargo complex (Figure 8C). This model integrates the common observation of slow transport being kinesin dependent (Terada et al., 2000; Uchida et al., 2009) with the fact that almost all kinesin-1 moves within the fast component of axonal transport (Elluru et al., 1995).

In summary, our kinesin-limited model implies that SCb cargos have a limited ability to recruit and hold kinesin in an active cargo-bound state, within a cytosolic environment with a limited supply of available active kinesin motors (Figure 8). The concept of sporadic transport by “fast” motors underlies all three models for slow axonal transport: “stop and go,” “dynamic recruitment,” and “kinesin limited.” However, our model is distinct from the previous models as it is neither polymer mediated (as for assembled neurofilaments), nor vesicle associated (as for synapsin).

The study of slow axonal transport is challenging due to the slow timescale of the overall transport rates and the indistinct nature of the transport unit for cytosolic cargoes. We have established that the anterograde slow axonal transport of dynein is dependent on direct interactions with kinesin. In doing so, we have established the first set of molecular-level details for a cytosolic slow transport complex, which can now be used to probe the underlying principles of slow axonal transport; in particular, providing insights into the difference between kinesin recruitment for slow compared to fast axonal transport. This work elucidates the dynamic nature of dynein localization in neurons and the mechanism of dynein’s anterograde axonal transport, a critical cellular motor whose function is required up to 1 m from the soma.

EXPERIMENTAL PROCEDURES

Details of antibodies, cDNA constructs, yeast two-hybrid assay, cell culture, fixed cell imaging, and co-immunoprecipitation can be found in the [Supplemental Experimental Procedures](#).

Live Cell Imaging

Live cell imaging of hippocampal cultures was performed in Hibernate E low fluorescence medium in a humidified temperature controlled (37°C) live cell chamber, on an Ultraview Vox (PerkinElmer) dual-imaging system mounted on an inverted Nikon Ti microscope with either 100 \times or 60 \times apochromat 1.49 NA oil-immersion objectives (Nikon), fully controlled by Volocity software (PerkinElmer). FRAP and slow axonal transport imaging used the spinning-disk confocal with an Ultraview Photokinesis unit for bleaching and a C9100-50 EM-CCD (Hamamatsu) camera. Near-TIRF imaging used the Nikon TIRF system with an EM-CCD C9100-13 camera (Hamamatsu). Image analysis was performed in FIJI (Schindelin et al., 2012) with follow up analysis in R (RStudio). Specifics for each experiment are listed in the [Supplemental Experimental Procedures](#).

Fluorescence Polarization Measurements

Measurements were performed as previously described (Pernigo et al., 2013) with modifications as listed in [Supplemental Experimental Procedures](#).

Sucrose Gradient Fractionation

Four mouse brains were homogenized in 16 mL of ice-cold Homogenization buffer (10 mM HEPES [pH 7.4], 0.32 M sucrose, 2 mM EDTA plus protease inhibitors) and subjected to differential centrifugation steps outlined in [Supplemental Experimental Procedures](#). 15%–45% sucrose gradients (15% or 45% sucrose in 10 mM HEPES [pH 7.4], 2 mM EDTA and protease inhibitors) had a 12 mL final volume and 0.5 mL fractions were taken from the top of the gradient for SDS-PAGE and western blotting. Protein concentration and turbidity of fractions was analyzed at 280 and 340 nm, respectively, in a SynergyMx plate reader (BioTek).

For [Figure S4A](#), cytoplasmic dynein and kinesin from the cytosolic pool (S3) was enriched from the brains of adult mice by microtubule affinity and ATP release, followed by sucrose density gradient centrifugation as previously described (Ayloo et al., 2014). Equal fraction volumes were separated by SDS-PAGE and transferred to immobilon-PVDF membrane (Millipore) for western blotting.

Single Molecule TIRFM Imaging

Flow chambers were formed of a glass slide and silanized (PlusOne Repel Silane, GE Healthcare) coverslip, sandwiched together with adhesive tape and bordered with vacuum grease. Chamber volume was $\sim 10 \mu\text{L}$. The flow chamber was coated with a 1:50 dilution of the monoclonal anti-tubulin antibody (Sigma) then blocked with 5% pluronic F-127 (Sigma). Dual-labeled (AMCA-labeled tubulin seeds with rhodamine tubulin extensions, Cytoskeleton) taxol-stabilized microtubules were flowed into the chamber and allowed to bind the anti-tubulin antibody. The appropriate fraction from the sucrose gradient was supplemented with Mg-ATP (1 mM), bovine serum albumin (1 mg/mL), casein (1 mg/mL), taxol (20 μM), DTT (1 mM), glucose (140 mM), and a glucose catalase/oxidase anti-fade system. Imaging was performed with Ultraview Vox (PerkinElmer) system with 100 \times apochromat 1.49 NA oil-immersion objective (Nikon). Chambers were imaged at 3–5 frames per second.

Analysis

All numerical analysis and plotting were performed in R (RStudio), with additional packages dplyr, reshape2, and ggplot2. Statistical comparisons were performed with base R functions as independent (unpaired) t tests, with Bonferroni correction where multiple comparisons were performed ([Figures 3G and 3I](#)).

SUPPLEMENTAL INFORMATION

Supplemental Information includes Supplemental Experimental Procedures, five figures, and three movies and can be found with this article online at <http://dx.doi.org/10.1016/j.neuron.2016.04.046>.

A video abstract is available at <http://dx.doi.org/10.1016/j.neuron.2016.04.046#mmc6>.

AUTHOR CONTRIBUTIONS

A.E.T., G.S., and E.L.F.H. conceived the project and designed experiments. S.P., A.S., R.A.S., and M.P.D. performed and analyzed fluorescence

polarization measurements; P.G.-D. performed and analyzed anti-DIC immunofluorescence; A.E.T. performed and analyzed all other experiments. A.E.T. and E.L.F.H. wrote the manuscript. All authors reviewed and edited the manuscript.

ACKNOWLEDGMENTS

We gratefully acknowledge Mariko Tokito and Karen Jahn for their technical assistance and Sandra Maday, Swathi Ayloo, Meredith Wilson, and Adam Hendricks for helpful discussions as well as all members of the E.L.F.H. laboratory for help and encouragement. We also acknowledge Daniel Bose for extensive discussion and comments on the manuscript. This work is supported by funding from NIH grant GM48661 to E.L.F.H. A.E.T. is supported by a Sir Henry Wellcome Postdoctoral Fellowship (Wellcome Trust grant 096141/Z/11/Z).

Received: December 7, 2015

Revised: March 11, 2016

Accepted: April 18, 2016

Published: May 19, 2016

REFERENCES

- Ayloo, S., Lazarus, J.E., Dodda, A., Tokito, M., Ostap, E.M., and Holzbaur, E.L.F. (2014). Dynactin functions as both a dynamic tether and brake during dynein-driven motility. *Nat. Commun.* **5**, 4807.
- Baas, P.W., Black, M.M., and Banker, G.A. (1989). Changes in microtubule polarity orientation during the development of hippocampal neurons in culture. *J. Cell Biol.* **109**, 3085–3094.
- Brown, A., Wang, L., and Jung, P. (2005). Stochastic simulation of neurofilament transport in axons: the “stop-and-go” hypothesis. *Mol. Biol. Cell* **16**, 4243–4255.
- Dillman, J.F., 3rd, Dabney, L.P., Karki, S., Paschal, B.M., Holzbaur, E.L.F., and Pfister, K.K. (1996a). Functional analysis of dynactin and cytoplasmic dynein in slow axonal transport. *J. Neurosci.* **16**, 6742–6752.
- Dillman, J.F., 3rd, Dabney, L.P., and Pfister, K.K. (1996b). Cytoplasmic dynein is associated with slow axonal transport. *Proc. Natl. Acad. Sci. USA* **93**, 141–144.
- Dodding, M.P., Mitter, R., Humphries, A.C., and Way, M. (2011). A kinesin-1 binding motif in vaccinia virus that is widespread throughout the human genome. *EMBO J.* **30**, 4523–4538.
- Egan, M.J., McClintock, M.A., and Reck-Peterson, S.L. (2012a). Microtubule-based transport in filamentous fungi. *Curr. Opin. Microbiol.* **15**, 637–645.
- Egan, M.J., Tan, K., and Reck-Peterson, S.L. (2012b). Lis1 is an initiation factor for dynein-driven organelle transport. *J. Cell Biol.* **197**, 971–982.
- Elluru, R.G., Bloom, G.S., and Brady, S.T. (1995). Fast axonal transport of kinesin in the rat visual system: functionality of kinesin heavy chain isoforms. *Mol. Biol. Cell* **6**, 21–40.
- Encalada, S.E., Szpankowski, L., Xia, C.-H., and Goldstein, L.S.B. (2011). Stable kinesin and dynein assemblies drive the axonal transport of mammalian prion protein vesicles. *Cell* **144**, 551–565.
- Friedman, D.S., and Vale, R.D. (1999). Single-molecule analysis of kinesin motility reveals regulation by the cargo-binding tail domain. *Nat. Cell Biol.* **1**, 293–297.
- Fu, M.-M., and Holzbaur, E.L.F. (2013). JIP1 regulates the directionality of APP axonal transport by coordinating kinesin and dynein motors. *J. Cell Biol.* **202**, 495–508.
- Fu, M.-M., and Holzbaur, E.L.F. (2014). Integrated regulation of motor-driven organelle transport by scaffolding proteins. *Trends Cell Biol.* **24**, 564–574.
- Garner, J.A., and Lasek, R.J. (1982). Cohesive axonal transport of the slow component b complex of polypeptides. *J. Neurosci.* **2**, 1824–1835.
- Garner, J.A., and Mahler, H.R. (1987). Biogenesis of presynaptic terminal proteins. *J. Neurochem.* **49**, 905–915.
- Grabham, P.W., Seale, G.E., Benneceib, M., Goldberg, D.J., and Vallee, R.B. (2007). Cytoplasmic dynein and LIS1 are required for microtubule advance during growth cone remodeling and fast axonal outgrowth. *J. Neurosci.* **27**, 5823–5834.
- Grafstein, B., McEwen, B.S., and Shelanski, M.L. (1970). Axonal transport of neurotubule protein. *Nature* **227**, 289–290.
- Hackney, D.D., Levitt, J.D., and Suhan, J. (1992). Kinesin undergoes a 9 S to 6 S conformational transition. *J. Biol. Chem.* **267**, 8696–8701.
- He, Y., Francis, F., Myers, K.A., Yu, W., Black, M.M., and Baas, P.W. (2005). Role of cytoplasmic dynein in the axonal transport of microtubules and neurofilaments. *J. Cell Biol.* **168**, 697–703.
- Heerssen, H.M., Pazyra, M.F., and Segal, R.A. (2004). Dynein motors transport activated Trks to promote survival of target-dependent neurons. *Nat. Neurosci.* **7**, 596–604.
- Hendricks, A.G., Perlson, E., Ross, J.L., Schroeder, H.W., 3rd, Tokito, M., and Holzbaur, E.L.F. (2010). Motor coordination via a tug-of-war mechanism drives bidirectional vesicle transport. *Curr. Biol.* **20**, 697–702.
- Hoffman, P.N., and Lasek, R.J. (1975). The slow component of axonal transport. Identification of major structural polypeptides of the axon and their generality among mammalian neurons. *J. Cell Biol.* **66**, 351–366.
- Jacobson, C., Schnapp, B., and Banker, G.A. (2006). A change in the selective translocation of the Kinesin-1 motor domain marks the initial specification of the axon. *Neuron* **49**, 797–804.
- Klein, J.A., Bruneau, R., Calder, K., Pocock, D., VandenBerg, P.M., MacDonald, E., Monfils, M.H., Sutherland, R.J., and Nader, K. (2003). Functional organization of adult motor cortex is dependent upon continued protein synthesis. *Neuron* **40**, 167–176.
- Kuta, A., Deng, W., Morsi El-Kadi, A., Banks, G.T., Hafezparast, M., Pfister, K.K., and Fisher, E.M.C. (2010). Mouse cytoplasmic dynein intermediate chains: identification of new isoforms, alternative splicing and tissue distribution of transcripts. *PLoS ONE* **5**, e11682.
- Lenz, J.H., Schuchardt, I., Straube, A., and Steinberg, G. (2006). A dynein loading zone for retrograde endosome motility at microtubule plus-ends. *EMBO J.* **25**, 2275–2286.
- Ligon, L.A., Tokito, M., Finklestein, J.M., Grossman, F.E., and Holzbaur, E.L.F. (2004). A direct interaction between cytoplasmic dynein and kinesin I may coordinate motor activity. *J. Biol. Chem.* **279**, 19201–19208.
- Lloyd, T.E., Machamer, J., O'Hara, K., Kim, J.H., Collins, S.E., Wong, M.Y., Sahin, B., Imlach, W., Yang, Y., Levitan, E.S., et al. (2012). The p150(Glued) CAP-Gly domain regulates initiation of retrograde transport at synaptic termini. *Neuron* **74**, 344–360.
- Maday, S., Wallace, K.E., and Holzbaur, E.L.F. (2012). Autophagosomes initiate distally and mature during transport toward the cell soma in primary neurons. *J. Cell Biol.* **196**, 407–417.
- Maday, S., Twelvetrees, A.E., Moughamian, A.J., and Holzbaur, E.L.F. (2014). Axonal transport: cargo-specific mechanisms of motility and regulation. *Neuron* **84**, 292–309.
- Moughamian, A.J., and Holzbaur, E.L.F. (2012). Dynactin is required for transport initiation from the distal axon. *Neuron* **74**, 331–343.
- Moughamian, A.J., Osborn, G.E., Lazarus, J.E., Maday, S., and Holzbaur, E.L.F. (2013). Ordered recruitment of dynactin to the microtubule plus-end is required for efficient initiation of retrograde axonal transport. *J. Neurosci.* **33**, 13190–13203.
- Myers, K.A., Tint, I., Nadar, C.V., He, Y., Black, M.M., and Baas, P.W. (2006). Antagonistic forces generated by cytoplasmic dynein and myosin-II during growth cone turning and axonal retraction. *Traffic* **7**, 1333–1351.
- Nirschl, J.J., Magiera, M.M., Lazarus, J.E., Janke, C., and Holzbaur, E.L.F. (2016). α -Tubulin Tyrosination and CLIP-170 Phosphorylation Regulate the Initiation of Dynein-Driven Transport in Neurons. *Cell Rep.* **14**, 2637–2652.
- Perlson, E., Hendricks, A.G., Lazarus, J.E., Ben-Yaakov, K., Gradus, T., Tokito, M., and Holzbaur, E.L.F. (2013). Dynein interacts with the neural cell adhesion molecule (NCAM180) to tether dynamic microtubules and maintain synaptic density in cortical neurons. *J. Biol. Chem.* **288**, 27812–27824.

- Pernigo, S., Lamprecht, A., Steiner, R.A., and Dodding, M.P. (2013). Structural basis for kinesin-1:cargo recognition. *Science* **340**, 356–359.
- Pilling, A.D., Horiuchi, D., Lively, C.M., and Saxton, W.M. (2006). Kinesin-1 and Dynein are the primary motors for fast transport of mitochondria in *Drosophila* motor axons. *Mol. Biol. Cell* **17**, 2057–2068.
- Roberts, A.J., Goodman, B.S., and Reck-Peterson, S.L. (2014). Reconstitution of dynein transport to the microtubule plus end by kinesin. *eLife* **3**, e02641.
- Roossien, D.H., Lamoureux, P., and Miller, K.E. (2014). Cytoplasmic dynein pushes the cytoskeletal meshwork forward during axonal elongation. *J. Cell Sci.* **127**, 3593–3602.
- Ross, J.L., Wallace, K., Shuman, H., Goldman, Y.E., and Holzbaur, E.L.F. (2006). Processive bidirectional motion of dynein-dynactin complexes in vitro. *Nat. Cell Biol.* **8**, 562–570.
- Roy, S. (2014). Seeing the unseen: the hidden world of slow axonal transport. *Neuroscientist* **20**, 71–81.
- Roy, S., Coffee, P., Smith, G., Liem, R.K., Brady, S.T., and Black, M.M. (2000). Neurofilaments are transported rapidly but intermittently in axons: implications for slow axonal transport. *J. Neurosci.* **20**, 6849–6861.
- Schiavo, G., Greensmith, L., Hafezparast, M., and Fisher, E.M.C. (2013). Cytoplasmic dynein heavy chain: the servant of many masters. *Trends Neurosci.* **36**, 641–651.
- Schindelin, J., Arganda-Carreras, I., Frise, E., Kaynig, V., Longair, M., Pietzsch, T., Preibisch, S., Rueden, C., Saalfeld, S., Schmid, B., et al. (2012). Fiji: an open-source platform for biological-image analysis. *Nat. Methods* **9**, 676–682.
- Scott, D.A., Das, U., Tang, Y., and Roy, S. (2011). Mechanistic logic underlying the axonal transport of cytosolic proteins. *Neuron* **70**, 441–454.
- Tang, Y., Scott, D., Das, U., Gitler, D., Ganguly, A., and Roy, S. (2013). Fast vesicle transport is required for the slow axonal transport of synapsin. *J. Neurosci.* **33**, 15362–15375.
- Terada, S., Kinjo, M., and Hirokawa, N. (2000). Oligomeric tubulin in large transporting complex is transported via kinesin in squid giant axons. *Cell* **103**, 141–155.
- Trivedi, N., Jung, P., and Brown, A. (2007). Neurofilaments switch between distinct mobile and stationary states during their transport along axons. *J. Neurosci.* **27**, 507–516.
- Uchida, A., Alami, N.H., and Brown, A. (2009). Tight functional coupling of kinesin-1A and dynein motors in the bidirectional transport of neurofilaments. *Mol. Biol. Cell* **20**, 4997–5006.
- Wagner, O.I., Ascaño, J., Tokito, M., Leterrier, J.-F., Janmey, P.A., and Holzbaur, E.L.F. (2004). The interaction of neurofilaments with the microtubule motor cytoplasmic dynein. *Mol. Biol. Cell* **15**, 5092–5100.
- Wang, L., Ho, C.L., Sun, D., Liem, R.K., and Brown, A. (2000). Rapid movement of axonal neurofilaments interrupted by prolonged pauses. *Nat. Cell Biol.* **2**, 137–141.
- Williams, L.S., Ganguly, S., Loiseau, P., Ng, B.F., and Palacios, I.M. (2014). The auto-inhibitory domain and ATP-independent microtubule-binding region of Kinesin heavy chain are major functional domains for transport in the *Drosophila* germline. *Development* **141**, 176–186.
- Xia, C.-H., Roberts, E.A., Her, L.-S., Liu, X., Williams, D.S., Cleveland, D.W., and Goldstein, L.S.B. (2003). Abnormal neurofilament transport caused by targeted disruption of neuronal kinesin heavy chain KIF5A. *J. Cell Biol.* **161**, 55–66.
- Yamada, M., Toba, S., Yoshida, Y., Haratani, K., Mori, D., Yano, Y., Mimori-Kiyosue, Y., Nakamura, T., Itoh, K., Fushiki, S., et al. (2008). LIS1 and NDEL1 coordinate the plus-end-directed transport of cytoplasmic dynein. *EMBO J.* **27**, 2471–2483.
- Yano, H., Lee, F.S., Kong, H., Chuang, J., Arevalo, J., Perez, P., Sung, C., and Chao, M.V. (2001). Association of Trk neurotrophin receptors with components of the cytoplasmic dynein motor. *J. Neurosci.* **21**, RC125.
- Zhang, J., Li, S., Fischer, R., and Xiang, X. (2003). Accumulation of cytoplasmic dynein and dynactin at microtubule plus ends in *Aspergillus nidulans* is kinesin dependent. *Mol. Biol. Cell* **14**, 1479–1488.
- Zhang, J., Twelvetrees, A.E., Lazarus, J.E., Blasier, K.R., Yao, X., Inamdar, N.A., Holzbaur, E.L.F., Pfister, K.K., and Xiang, X. (2013). Establishing a novel knock-in mouse line for studying neuronal cytoplasmic dynein under normal and pathologic conditions. *Cytoskeleton (Hoboken)* **70**, 215–227.

Neuron, Volume 90

Supplemental Information

**The Dynamic Localization of Cytoplasmic Dynein
in Neurons Is Driven by Kinesin-1**

Alison E. Twelvetrees, Stefano Pernigo, Anneri Sanger, Pedro Guedes-Dias, Giampietro Schiavo, Roberto A. Steiner, Mark P. Dodding, and Erika L.F. Holzbaur

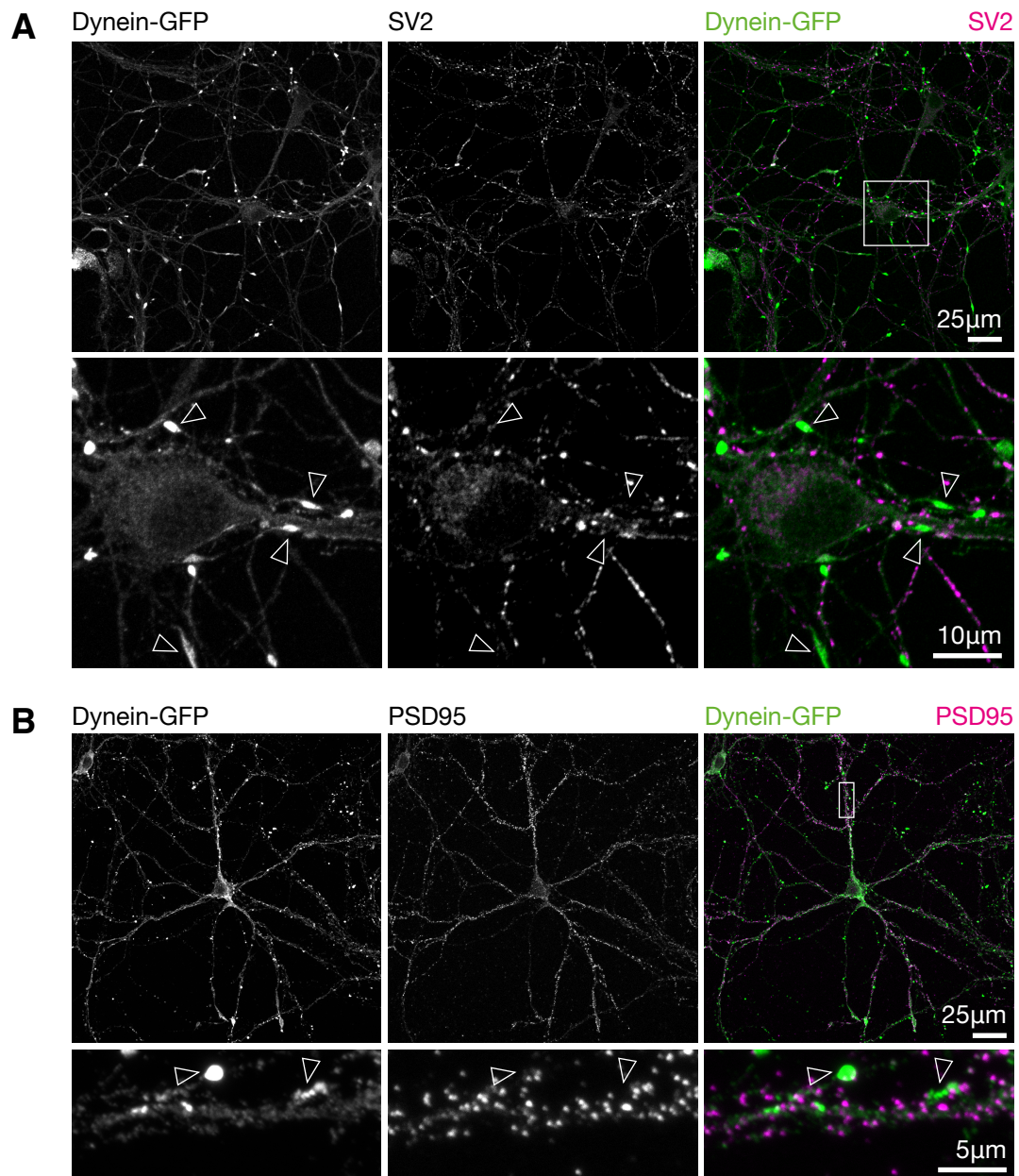


Figure S1. Related to Figure 1.

(A) Dynein-GFP is not enriched at pre-synaptic sites. Immunofluorescence and confocal microscopy of 8 DIV primary hippocampal neurons shows dynein-GFP accumulation does not colocalise with the presynaptic marker SV2 (empty arrowheads).

(B) Dynein-GFP is not enriched at post-synaptic sites. Immunofluorescence and confocal microscopy of mature 21 DIV primary hippocampal neurons shows dynein-GFP axonal foci do not colocalise with the postsynaptic marker PSD-95 (empty arrowheads).

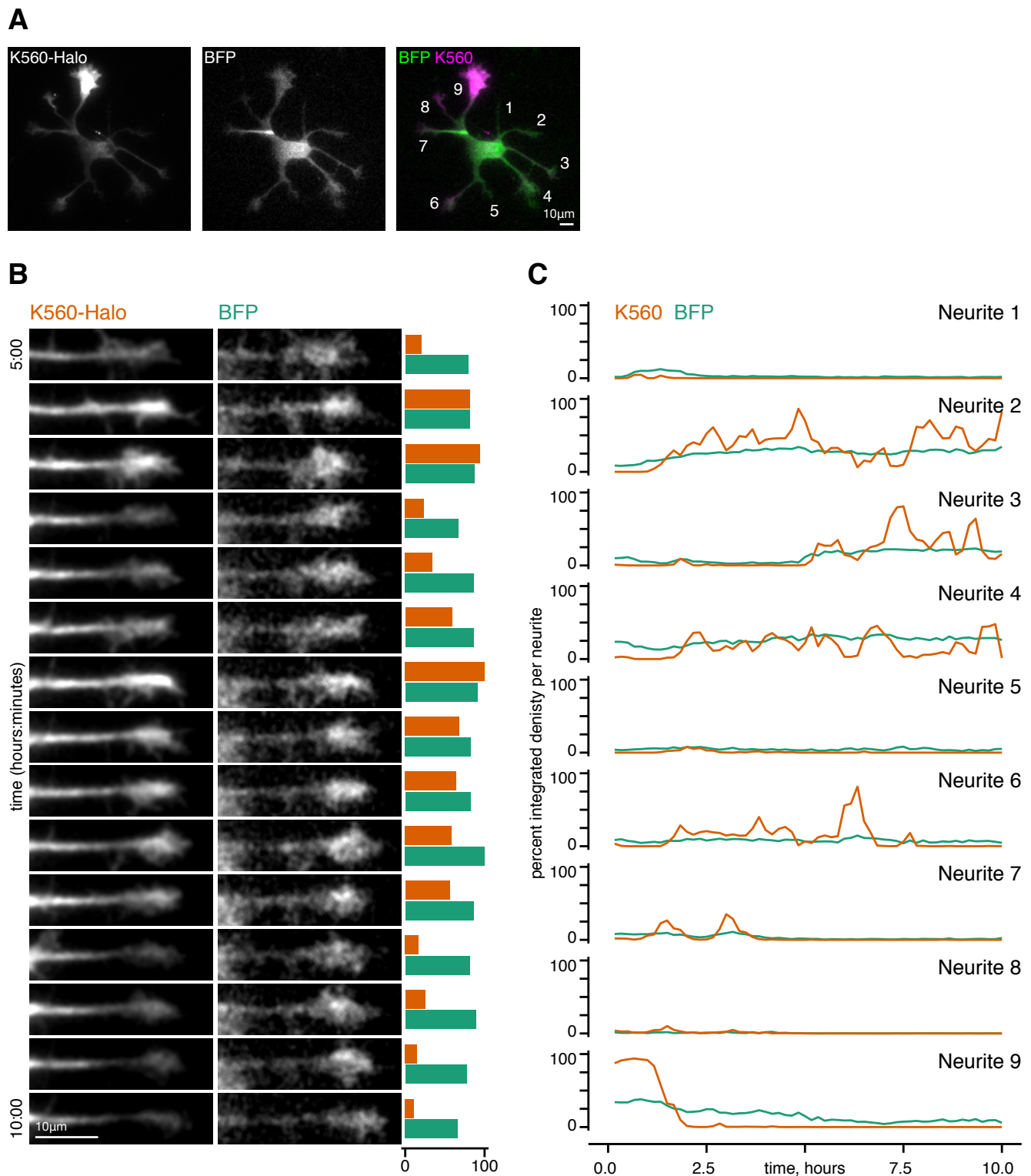


Figure S2. Related to Figure 2.

(A) Dynein-GFP neuron transfected with the cytosolic marker BFP. Maximum projection of all frames in Movie S3 indicating neurite labelling used for quantification in B-C. Scale bar, 10 μm .

(B) The movement of dynein-GFP within developing neurites is not mirrored by BFP. Still images of Neurite 4 from (A) through time. Quantification bars to the right show the relative integrated density of fluorescence for K560-Halo (orange) and BFP (green) within Neurite 4 over time. Scale bar, 10 μm .

(C) The movement of dynein-GFP across developing neurites is not mirrored by BFP. Quantification of the neurite intensity as a percentage of the total in all neurites through time, demonstrating the absence of BFP accumulation in any one neurite relative to other developing neurites labelled in D.

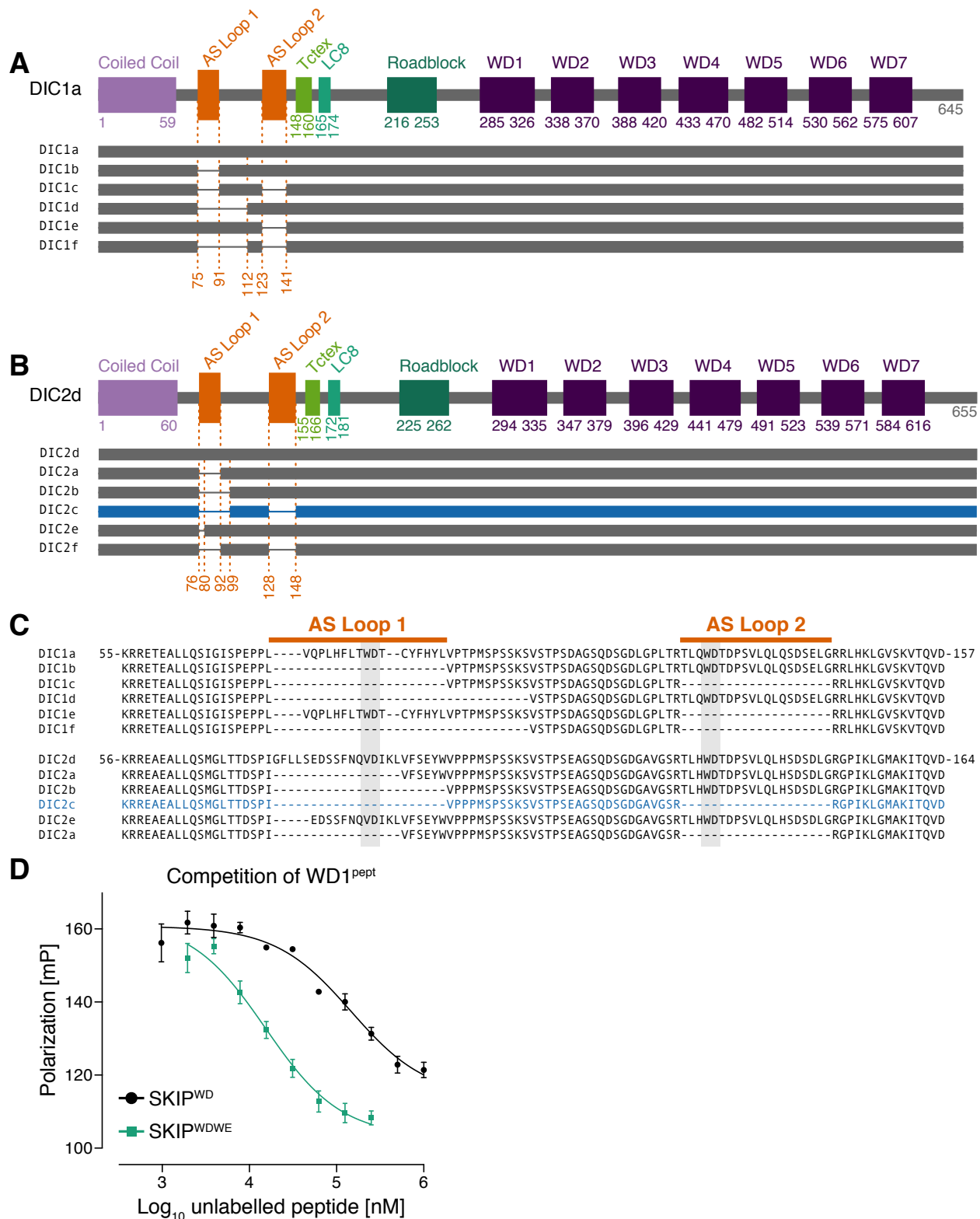
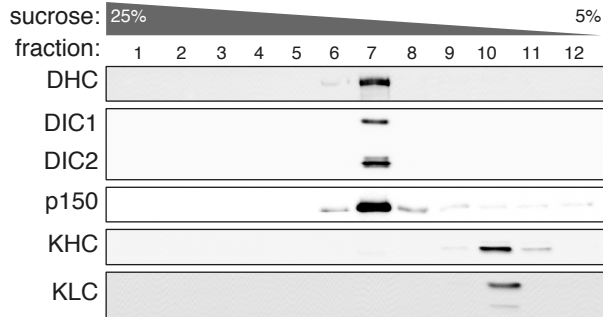
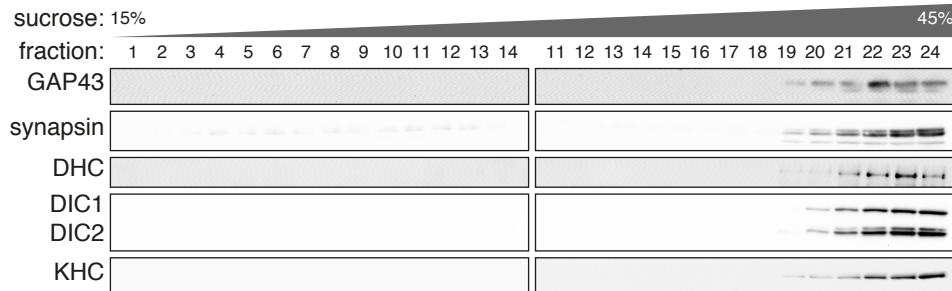
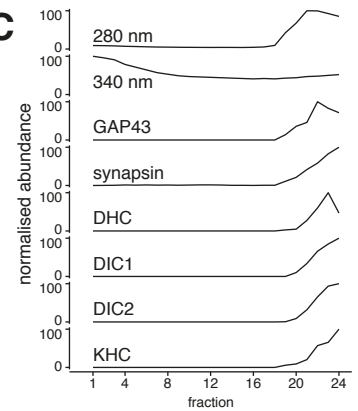


Figure S3. Related to Figure 3.

(A-C) Isoforms of the mouse cytoplasmic dynein intermediate chain, based on data from (Kuta et al., 2010). The splice forms of DIC1 (A) and DIC2 (B) from the genes *Dync1i1* and *Dync1i2* respectively, relative to the longest isoform of each with key structural elements indicated: coiled coil required for NudE and p150 binding (McKenney et al., 2011; Nyarko et al., 2012); binding sites of the dynein light chains Tctex (Mok et al., 2001), LC8 (Lo et al., 2001) and Roadblock (Susalka et al., 2002); WD repeats 1-7 of the WD40 domain. Sequence alignments of all DIC isoforms centred on the two alternatively spliced regions: AS Loop 1 and AS Loop 2 (C). The location of the two tryptophan motifs within both alternatively spliced regions are highlighted in grey. The ubiquitous DIC isoform, DIC2c, is shown in blue. DIC2c does not contain either AS Loop 1 or 2.

(D) In a fluorescence polarization competition assay, TAMRA-labeled WD1^{pept} bound to KLC1^{TPR} is competed off with both unlabeled SKIP^{WD} (with a single tryptophan motif) or a longer peptide encompassing both motifs (SKIP^{WDWE}). Both SKIP peptides compete off WD1^{pept} in a concentration dependent manner, with the longer and higher affinity SKIP^{WDWE} peptide doing so more efficiently. The sequence of all peptides used is in Supplemental Experimental Procedures. Error bars \pm sem, experiments typically done in triplicate.

A**B****C****Figure S4. Related to Figure 5.**

Biochemical Analysis of endogenous dynein-GFP and kinesin complexes from brain.

(A) Microtubule motors enriched from the cytoplasmic (S3) fraction of brain lysate by their ability to bind microtubules, subsequently separated by sucrose gradient. Dynein and kinesin motors do not co-migrate in this preparation.

(B) Density gradient assay of the resuspended P3 fraction performed in parallel to that in Figure 5D, but in the presence of Triton-X-100 to solubilise vesicles. Protein that was previously floating in less dense fractions of the gradient (see Figure 5D) as part of the vesicle fraction is now collapsed into the high density fractions at the bottom of the gradient.

(C) Quantification of the gradient assay in (A) showing the absence of the vesicular associated protein in fractions 10-19.

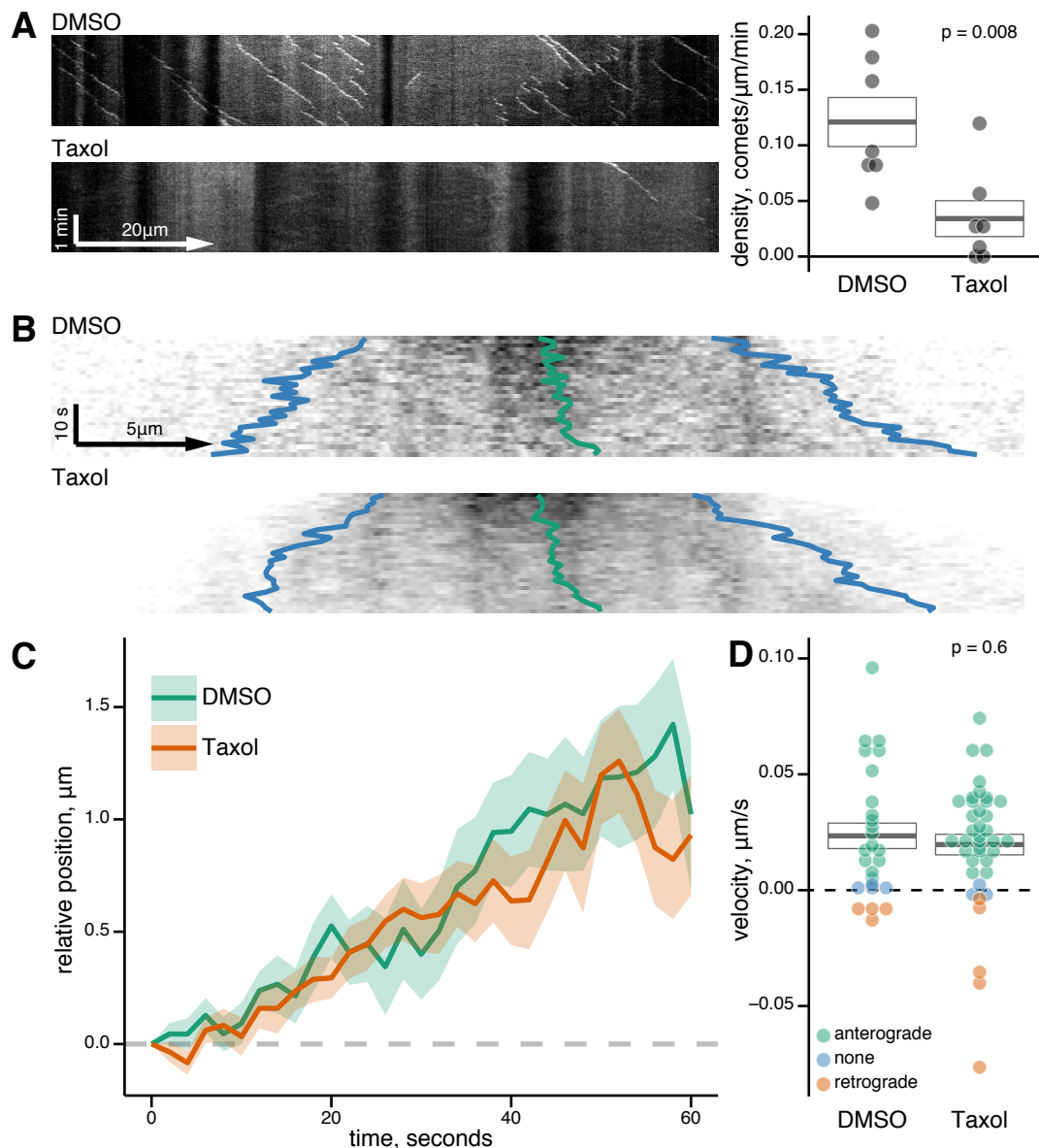


Figure S5. Related to Figure 7.

The slow anterograde transport of dynein in the axon is not dependent on dynamic microtubules.

(A) Taxol treatment reduces the density of EB3 comets in the axon. Example kymographs (left) and quantification (right) of EB3-mCherry comet density in DMSO control and taxol treated axons. Pre-treatment with taxol (200 nM final concentration) for 45-60 minutes prior to imaging reduces the density of EB3 comets in the axon from 0.12 to 0.03 comets/ $\mu\text{m}/\text{min}$. Heavy line = mean, box = sem, grey dots = individual axons. Axons were imaged at 1 frame per second for 3 minutes using live cell spinning disk confocal microscopy.

(B) Example slow axonal transport kymographs of DMSO control and taxol treated axons from dynein-GFP hippocampal neurons showing relative positions of anterograde and retrograde intercept (blue) and the calculated midpoint displacement (green) following the bleaching protocol used to analyse slow axonal transport (see Figure 6).

(C) Quantification of the midpoint displacement shows that taxol treatment has no effect on the anterograde bias of dynein-GFP transport in the axon. The mean relative position of the midpoint with time for DMSO and taxol treated axons: n = 26 and 39 axons respectively from 3 independent primary cultures; solid lines, mean; ribbons, \pm sem.

(D) The mean velocity of dynein displacement in the axon is unaffected by taxol treatment. A linear regression was fitted to each midpoint displacement to find the velocity of displacement. The mean velocity (heavy line) \pm sem (box) is shown. Overlaid spots are the velocities for each measured kymograph with colour indicating the overall direction of the midpoint displacement. Taxol treatment causes no changes to the mean velocity of anterograde displacement. DMSO mean velocity $0.023 \pm 0.005 \mu\text{m}/\text{s}$; Taxol mean velocity $0.020 \pm 0.004 \mu\text{m}/\text{s}$. p value calculated by a two-sample t-test.

Movie S1. Related to Figure 2.

Neurite outgrowth in a dynein-GFP stage 2 hippocampal neuron imaged overnight. Time stamp, hours:minutes. Fluorescence intensity scale as for Figure 2A.

Movie S2. Related to Figure 2.

Neurite outgrowth in dynein-GFP in stage 2 hippocampal neuron transfected with constitutively active K560-Halo and imaged overnight. Time stamp, hours:minutes. Left panel, K560-Halo; Middle panel, dynein-GFP; Right panel, K560-Halo (magenta) and dynein-GFP (green) merge.

Movie S3. Related to Figure S2.

Neurite outgrowth in stage 2 hippocampal neuron transfected with both K560-Halo and BFP and imaged overnight. Time stamp, hours:minutes. Left panel, K560-Halo; Middle panel, BFP; Right panel, K560-Halo (magenta) and BFP (green) merge.

Supplemental Experimental Procedures

Antibodies

Primary antibodies used: chicken anti-GFP (Aves Labs, GFP-1020); mouse anti-mCherry (Living Colors, 632543); mouse anti-FLAG(M2) (Sigma, F1804); rabbit anti-Tau (Abcam); mouse anti-SV2 (recognises all three SV2 isoforms); mouse anti-DIC (Millipore, MAB1618); rabbit anti-GAP43 (Chemicon, MAB 347); anti-PSD95 (Millipore, MAB1596); rabbit anti-synapsin; rabbit anti-DHC (Santa Cruz); mouse anti-p150 (BD biosciences, 610474); mouse anti-KHC/KIF5 (Millipore, MAB1614); mouse anti-KLC (Millipore, MAB1616); rabbit anti-KLC2 (Abcam, ab116702).

Fluorophore conjugated secondary antibodies were Cy2 conjugated goat anti-chicken (Jackson) or goat anti-chicken Alexa 488 (ThermoFisher); and goat anti-rabbit Alexa 594 (Invitrogen), anti-mouse Alexa 594 (Invitrogen) or goat anti-mouse Alexa 555 (ThermoFisher). HRP conjugated secondary antibodies were from Jackson.

cDNA Constructs

All kinesin constructs used have been previously described (Fu and Holzbaur, 2013; Ligon et al., 2004; Twelvetrees et al., 2010). The DIC1a construct was originally a gift from Richard Vallee. mCherry tagged DIC1a was made by replacing the EGFP tag in pEGFP-N1 with mCherry. Site-directed mutagenesis was carried out with Agilent (Stratagene) OC lightning Multi Side-directed Mutagenesis Kit following manufacturers instructions. Every base of mutant constructs was confirmed by sequencing.

Yeast two-hybrid assay

Previous studies have demonstrated a direct interaction between DIC1 and either KLC1 or KLC2 (Ligon et al., 2004). In a yeast two-hybrid assay to screen a random-primed human fetal brain cDNA library for further interactors of DIC1 as described in (Perlson et al., 2013), we identified a cDNA encoding residues 389-637 of KIF5A as a possible interaction partner. Interactions between DIC1A and KIF5A, KIF5B, and KIF5C were verified by co-immunoprecipitation experiments, while the binding domain within KIF5C was identified by comparing co-precipitation of mCherry-DIC1 with KIF5C head, stalk, and tail constructs.

Primary hippocampal neuronal culture

Hippocampal neurons were isolated from E15.5 dynein-GFP mice and cultured as previously described (Zhang et al., 2013). For microfluidic chambers (RD900, Xona Microfluidics) 300,000 neurons were seeded into each chamber and maintained by exchange of 30% of the maintenance media every day.

Immunocytochemistry and confocal imaging

Hippocampal neurons were fixed and stained as previously described (Twelvetrees et al., 2010). Figures 1B&C and S1A&B were imaged with Zeiss LSM 710 with a Plan-Apochromat 63x/1.40 NA oil immersion objective and are maximum projections of z-stacks taken at the recommended sampling rate with pinhole set to 1 Airy unit (planes that included just neuronal soma were excluded from the projection). Figures 1D-E were imaged using UltraVIEW VoX spinning-disk confocal microscope (PerkinElmer) with an Apochromat 100X, 1.49 NA oil immersion objective (Nikon). Digital images were acquired with C9100-50 EM-CCD camera (Hamamatsu). In order to show axon/dendritic labeling alongside bright puncta, images were contrast enhanced for presentation using FIJI/ImageJ. Tiling of overlapping fields of view in Figure 1D-E was done in ImageJ (D) or Photoshop (E). Pearson's correlation coefficient was calculated using Velocity software. Note that all dynein-GFP fixed cells were stained with anti-GFP antibodies to boost the GFP signal for confocal imaging.

Live cell imaging

FRAP

Photobleaching of dynein-GFP (Figure 1F) was performed with 488 nm laser at 100% power for 25 cycles using the 100X objective. Pre-bleach frames were acquired at 2 frames per second (2 fps), and post bleach frames at 2 frames per minute (fpm).

near-TIRF real time imaging

Axons were imaged with 100X objective and near-TIRF illumination with 488 nm laser. Frame rate was 3 fps for Figure 1G. Bleaching in Figure 1H was performed with the Ultraview Photokinesis device before switching to TIRF imaging mode and imaging recovery at 5 fps post bleaching.

Overnight live cell imaging

Cells were imaged with 60X objective with near-TIRF illumination to eliminate excessive fluorescence signal coming from out of focus soma. Acquisition was run overnight with frames acquired at 1 frame every ten minutes, with stage position controlled by Velocity software. For quantification, a threshold was applied to a maximum projection to define neurite regions of interest (ROI). These ROI were overlaid onto the movie and integrated density of each neurite was measured over time.

Slow axonal transport imaging and drug treatments

Axons were imaged with a 100X objective (Nikon). Acquisition speed was 1 frame every two seconds. For Nocodazole and Taxol drug treatments, 33 μ M and 200 nM respective final concentrations were added to each well of the microfluidic chamber in imaging media (Hibernate E Low Fluorescence media) 45-60 minutes prior to imaging, with hydrostatic pressure across the microgrooves of the microfluidic device to ensure drugs reached the axons within the grooves.

Peptides were supplied by GenScript, and sequences are VCFYLLLQWVFPYTHDLH and LVQPLHFLTWDTCYFHLYLV for Control and DIC1a-WD1 peptides respectively. For peptide treatments, 500 ng of peptide was complexed with Chariot reagent (Active Motif) following the manufacturer's instructions then applied to the chamber, immediately followed by imaging media. Peptide treated chambers were incubated for 60 minutes prior to imaging and peptides remained in the imaging media throughout the experiment.

Every suitable isolated axon within the chamber grooves was imaged. Axons without sufficient signal:noise to perform analysis were later discarded (see following). Kymographs of imaged axons were generated in FIJI (Schindelin et al., 2012): axons were straightened along a line the same width as the axon; straightened axons were re-sliced through the t-stack at 1 pixel intervals; 1 pixel kymographs were combined into the final kymograph with an average projection. Kymographs were analyzed with R (RStudio) using the following additional packages: TIFF kymograph images were imported into R using `tiff::readTIFF` (Urbanek, 2013); rolling average for each time point was performed with `zoo::rollapply` (Zeileis and Grothendieck, 2005); proximal and distal intercepts at half maximal intensity were calculated with the "approx" function; linear models were fitted with "lm"; additional data handling and plotting used the `dplyr` (Wickham and Francois, 2015) and `ggplot2` libraries respectively (Wickham, 2009). In order to obtain proximal and distal intercepts, the half maximal value has to be above background fluorescence in the axon; of the 31 frames analyzed for each movie, intercepts had to be calculated for at least 30 frames or the data was excluded.

Co-Immunoprecipitation

COS7 cells were passaged 24 hours prior to transfection with Eugene6 (Roche) according to the manufacturer's instructions, and harvested 16-24 hrs after transfection. One 10 cm plate of cells per condition was washed in PBS, transferred to a microcentrifuge tube and lysed in 1ml IP buffer (25 mM HEPES pH 7.4, 150 mM NaCl, 0.5% NP40, 0.5% Triton plus and protease inhibitor cocktail (Roche)) for ten minutes on ice. Cells lysate was harvested by centrifugation at 13,000 g for 10 min at 4°C. 1 μ g of antibody was added to lysate and incubated for 45 minutes at 4°C with rotation, followed by a further 15

minutes with the addition of 15 μ l of washed pre-equilibrated Protein-G Dynabeads. Beads were washed three times in IP buffer and then boiled in 50 μ l 1X SDS-loading buffer. Samples were separated by SDS-PAGE and transferred to immobilon-PVDF membrane (Millipore) for western blotting. Primary antibodies listed above. HRP conjugated secondary antibodies were from Jackson. Blots were visualized by detection of enhanced chemiluminescence (SuperSignal West Pico Chemiluminescent Substrate, Thermo Scientific) with a G:Box Chemi system controlled by GeneSys software (Syngene). Image analysis was performed in FIJI (Schindelin et al., 2012).

Fluorescence polarization measurements

N-terminal carboxytetramethylrhodamine (TAMRA) conjugated and unlabeled peptides were supplied by Bio-Synthesis Inc (Lewisville, TX, USA). Sequences are (WD^{1pept}: TAMRA-LHFLTWDTCYF, WD^{2pept}: TAMRA-TRTLQWDTDPS, SKIP^{WD}: STNLEWDDSAI, SKIP^{WDWE}: STNLEWDDSAIAPSSSEDYDFGDVFPVAVPSVPSTDWEDGDL). The TPR domain of KLC2 lacking the first helix of its first TPR repeat (KLC2^{TPR}, amino acids V218 to K480) was amplified from a mouse template and subcloned into the NdeI/XhoI sites of the pET28a vector (Novagen) to enable its expression with a thrombin-cleavable N-terminal hexa-histidine tag. All fluorescence polarization (FP) measurements were carried out on a BMG Labtech PolarStar Omega plate reader at 20 °C by incubating 300 nM TAMRA-labeled peptides with His6-tagged KLC2^{TPR} at increasing concentrations in 25 mM Hepes pH 7.5, 150 mM NaCl, 5 mM β -mercaptoethanol. Estimation of K_D 's assumed a one-site specific-binding model. For competition experiments a mixture of TAMRA-DIC^{WD1} and KLC2^{TPR} at 300 nM and 25 μ M, respectively (corresponding to approximately 70% saturation), were incubated with increasing concentrations of unlabeled SKIP^{WD} and SKIP^{WDWE} peptides. Concentration-dependent decrease in FP signal was fitted to sigmoidal curve. Analyses were performed using the Prism package (GraphPad Software Inc., San Diego CA, USA).

Sucrose gradient fractionation

Four mouse brains were homogenized in 16 ml of ice cold Homogenization buffer (10 mM HEPES pH 7.4, 0.32 M sucrose, 2 mM EDTA plus protease inhibitors) then centrifuged at 1000 g for 15 min at 4°C to form supernatant 'S1' and pellet 'P1'. S1 was centrifuged at 10,000g for 20 min at 4°C with an F21S-8x50y rotor in Sorval RC6+ centrifuge to form 'S2' and 'P2'. Supernatant S2 was centrifuged at ~100,000 x g for 60 min at 4°C in Beckman L7 Ultracentrifuge with 70.1 Ti rotor to form 'S3' and 'P3'. P3 was resuspended in 0.6 ml of Homogenization buffer with gentle strokes of a glass-Teflon homogenizer. Samples of S1-P3 were taken at each stage and protein content measured by BCA assay and normalized to 1 mg/ml with 10 μ g loaded on gels. P3 was then adjusted to 45% sucrose, and Triton-X-100 added to a final concentration of 1% to half of the sample. P3 fractions with and without Triton were bottom loaded onto 15-45% sucrose gradients (15% or 45% sucrose in 10 mM HEPES pH 7.4, 2 mM EDTA and protease inhibitors) with a 12 ml final volume and centrifuged at 160,000 x g for 16 hr at 4°C in Beckman L7 Ultracentrifuge with SW41 swinging bucket rotor. 0.5 ml fractions were taken from the top of the gradient. Protein concentration and turbidity of fractions was analyzed at 280 and 340 nm respectively in a SynergyMx plate reader (BioTek). Equal fraction volumes were separated by SDS-PAGE and transferred to immobilon-PVDF membrane (Millipore) for western blotting. Blots were visualized by detection of enhanced chemiluminescence (SuperSignal West Pico Chemiluminescent Substrate, Thermo Scientific) with a G:Box Chemi system controlled by GeneSys software (Syngene). Image analysis was performed in FIJI (Schindelin et al., 2012).

Supplemental References

- Fu, M.-M., Holzbaaur, E.L.F., 2013. JIP1 regulates the directionality of APP axonal transport by coordinating kinesin and dynein motors. *J Cell Biol* 202, 495–508. doi:10.1083/jcb.201302078
- Kuta, A., Deng, W., El-Kadi, A.M., Banks, G.T., Hafezparast, M., Pfister, K., Fisher, E.M.C., 2010. Mouse Cytoplasmic Dynein Intermediate Chains: Identification of New Isoforms, Alternative Splicing and Tissue Distribution of Transcripts. *PLoS ONE* 5, e11682. doi:10.1371/journal.pone.0011682
- Ligon, L.A., Tokito, M.K., Finklestein, J.M., Grossman, F.E., Holzbaaur, E.L.F., 2004. A direct interaction between cytoplasmic dynein and kinesin I may coordinate motor activity. *J Biol Chem* 279, 19201–19208. doi:10.1074/jbc.M313472200
- Lo, K.W., Naisbitt, S., Fan, J.S., Sheng, M., Zhang, M., 2001. The 8-kDa dynein light chain binds to its targets via a conserved (K/R)XTQT motif. *J Biol Chem* 276, 14059–14066. doi:10.1074/jbc.M010320200
- McKenney, R.J., Weil, S.J., Scherer, J., Vallee, R.B., 2011. Mutually exclusive cytoplasmic dynein regulation by NudE-Lis1 and dynactin. *J Biol Chem* 286, 39615–39622. doi:10.1074/jbc.M111.289017
- Mok, Y.K., Lo, K.W., Zhang, M., 2001. Structure of Tctex-1 and its interaction with cytoplasmic dynein intermediate chain. *J Biol Chem* 276, 14067–14074. doi:10.1074/jbc.M011358200
- Nyarko, A., Song, Y., Barbar, E., 2012. Intrinsic disorder in dynein intermediate chain modulates its interactions with NudE and dynactin. *J Biol Chem*. doi:10.1074/jbc.M112.376038
- Perlson, E., Hendricks, A.G., Lazarus, J.E., Ben-Yaakov, K., Gradus, T., Tokito, M.K., Holzbaaur, E.L.F., 2013. Dynein Interacts with the Neural Cell Adhesion Molecule (NCAM180) to Tether Dynamic Microtubules and Maintain Synaptic Density in Cortical Neurons. *J Biol Chem*. doi:10.1074/jbc.M113.465088
- Schindelin, J., Arganda-Carreras, I., Frise, E., Kaynig, V., Longair, M., Pietzsch, T., Preibisch, S., Rueden, C., Saalfeld, S., Schmid, B., Tinevez, J.-Y., White, D.J., Hartenstein, V., Eliceiri, K., Tomancak, P., Cardona, A., 2012. Fiji: an open-source platform for biological-image analysis. *Nat Methods* 9, 676–682. doi:doi:10.1038/nmeth.2019
- Susalka, S.J.S., Nikulina, K.K., Salata, M.W.M., Vaughan, P.S.P., King, S.M., Vaughan, K.T., Pfister, K., 2002. The roadblock light chain binds a novel region of the cytoplasmic Dynein intermediate chain. *J Biol Chem* 277, 32939–32946. doi:10.1074/jbc.M205510200
- Twelvetrees, A.E., Yuen, E.Y., Arancibia-Carcamo, I.L., Macaskill, A.F., Rostaing, P.P., Lumb, M.J., Humbert, S.S., Triller, A.A., Saudou, F., Yan, Z.Z., Kittler, J.T., 2010. Delivery of GABAARs to synapses is mediated by HAP1-KIF5 and disrupted by mutant huntingtin. *Neuron* 65, 53–65. doi:10.1016/j.neuron.2009.12.007
- Urbanek, S., 2013. tiff: Read and write TIFF images.
- Wickham, H., 2009. ggplot2: elegant graphics for data analysis.
- Wickham, H., Francois, R., 2015. dplyr: A grammar of data manipulation. R package version 04 02.
- Zeileis, A., Grothendieck, G., 2005. zoo: S3Infrastructure for Regular and Irregular Time Series. *J. Stat. Soft.* 14. doi:10.18637/jss.v014.i06
- Zhang, J., Twelvetrees, A.E., Lazarus, J.E., Blasier, K.R., Yao, X., Inamdar, N.A., Holzbaaur, E.L.F., Pfister, K., Xiang, X., 2013. Establishing a novel knock-in mouse line for studying neuronal cytoplasmic dynein under normal and pathologic conditions. *Cytoskeleton (Hoboken, NJ)* 70, 215–227. doi:10.1002/cm.21102